## Title

Interannual variability in North Atlantic weather: Data analysis and a quasi-geostrophic model



## Journal

Journal of the Atmospheric Sciences, 73(8)

## ISSN

0022-4928

## Authors

Feliks, Yizhak
Robertson, Andrew W
Ghil, Michael

## Publication Date

2016-08-01

## DOI

10.1175/jas-d-15-0297.1

Peer reviewed

# Interannual Variability in North Atlantic Weather: Data Analysis and a Quasigeostrophic Model

YIZHAK FELIKS

*Department of Atmospheric and Oceanic Sciences, and Institute of Geophysics and Planetary Physics, University of California, Los Angeles, Los Angeles, California*

ANDREW W. ROBERTSON

*International Research Institute for Climate and Society (IRI), Columbia University, Palisades, New York*

MICHAEL GHIL

*Department of Atmospheric and Oceanic Sciences, and Institute of Geophysics and Planetary Physics, University of California, Los Angeles, Los Angeles, California, and Geosciences Department, and Laboratoire de Météorologie Dynamique, CNRS, IPSL, Ecole Normale Supérieure, Paris, France*

(Manuscript received 2 October 2015, in final form 18 April 2016)

ABSTRACT

This paper addresses the effect of interannual variability in jet stream orientation on weather systems over the North Atlantic basin (NAB). The observational analysis relies on 65 yr of NCEP–NCAR reanalysis (1948–2012). The total daily kinetic energy of the geostrophic wind (GTKE) is taken as a measure of storm activity over the North Atlantic. The NAB is partitioned into four rectangular regions, and the winter average of GTKE is calculated for each quadrant. The spatial GTKE average over all four quadrants shows striking year-to-year variability and is strongly correlated with the North Atlantic Oscillation (NAO).

The GTKE strength in the northeast quadrant is closely related to the diffluence angle of the jet stream in the northwest quadrant. To gain insight into the relationship between the diffluence angle and its downstream impact, a quasigeostrophic baroclinic model is used. The results show that an initially zonal jet persists at its initial latitude over 30 days or longer, while a tilted jet propagates meridionally according to the Rossby wave group velocity, unless kept stationary by external forcing.

A Gulf Stream–like narrow sea surface temperature (SST) front provides the requisite forcing for an analytical steady-state solution to this problem. This SST front influences the atmospheric jet in the northwest quadrant: it both strengthens the jet and tilts it northward at higher levels, while its effect is opposite at lower levels. Reanalysis data confirm these effects, which are consistent with thermal wind balance. The results suggest that the interannual variability found in the GTKE may be caused by intrinsic variability of the thermal Gulf Stream front.

## 1. Introduction and motivation

The dynamics of interannual variability of midlatitude weather is a topic of longstanding meteorological interest. Blackmon (1976), Blackmon et al. (1984), and Hoskins et al. (1983) showed that the subannual atmospheric spectrum can be divided broadly into three time scales: short, intermediate, and long. The synoptic eddies whose time scale is less than 10 days are elongated in the north–south direction and found mainly near the jet exit, while the intermediate-time, 10–30-day patterns are more zonal and found mainly further downstream (e.g., centered over the North Atlantic).

On longer, 30–90-day time scales, one finds large-scale patterns associated with teleconnections. Over the North Atlantic, the most prominent of the latter—at least during the winter—is the North Atlantic Oscillation (NAO). The NAO's spatial pattern consists of a pressure dipole with its two centers over the Azores and Iceland, respectively,

*Corresponding author address*: Yizhak Feliks, Dept. of Mathematics, Israel Institute for Biological Research, P.O. Box 19, Ness-Ziona 70450, Israel.
E-mail: yizhakf@iibr.gov.il

DOI: 10.1175/JAS-D-15-0297.1

while its changes over time manifest themselves primarily by low-frequency variability on the order of a season or years (Barnston and Livezey 1987; Hurrell 1995; Lau 1988a; Rogers 1997; Hilmer and Jung 2000; Jung et al. 2003; Luo and Gong 2006; Johnson et al. 2008; Feliks et al. 2010, 2013). Luo et al. (2012) recently summarized studies of NAO subannual variability. Woollings et al. (2010a) showed that a good characterization of the changes in both strength and latitude of the jet stream's eddy-driven component requires the phase of the east Atlantic (EA) pattern in addition to the NAO; this pattern (Wallace and Gutzler 1981) consists of a pressure monopole over the North Atlantic with a center that lies between the two centers of the NAO dipole.

A long series of observational, theoretical, and GCM modeling studies since the 1970s have documented strong linkages between these frequency bands, emphasizing on the one hand the organizing influence of the lower frequencies on the synoptic-scale transients (Lau 1988b; Robertson and Metz 1989, 1990; Branstator 1995) and surface weather, as well as the impacts of these transient eddies on the former through upscale momentum flux convergence (Simmons and Hoskins 1978; Shutts 1983). For many years the NAO was thought to be unpredictable at the seasonal scale, but recent studies have found evidence of seasonal predictability of the NAO and associated European winter weather (Scaife et al. 2014).

Feliks et al. (2010, 2013) found that interannual oscillatory modes of the NAO index—while statistically significant—are weaker by an order of magnitude than its seasonal and subannual variability. Small as these lower-frequency and more systematic NAO variations may be, their impact on European weather is quite substantial (Hurrell et al. 2003; Wang et al. 2011). Feliks et al. (2004, 2011) provided a mechanism for the interannual variability of the Gulf Stream's SST front inducing interannual variability in the NAO that may, in turn, impact the storm track and downstream weather over Europe. Brachet et al. (2012) provided further evidence and details for this mechanism by studying it in the atmospheric general circulation model of the Laboratoire de Météorologie Dynamique in Paris and zooming in on its Gulf Stream region.

In the present paper, we follow up on this line of investigation and show that weak interannual variability in the diffluence angle of the jet stream in the western part of the North Atlantic basin (NAB) can lead to a large response on the weather scale in its eastern part. We show from reanalysis data that the correlation between the SST front—that is, the product of its gradient and the orientation angle—and the jet stream diffluence angle is high; furthermore, the latter has a strong interannual relationship with atmospheric eddy activity over the northeast (NE) Atlantic. By the analytical solution of an atmospheric baroclinic quasigeostrophic (QG) model we show that the SST front has a significant influence on the diffluence angle and can explain the observed change with height of this angle. We thus argue that the interannual variability found in weather in eastern part is caused by the interannual variability of the SST front.

The paper is organized as follows: In section 2, we consider the collective strength of the weather systems over the NAB as measured by the total kinetic energy over this region. This measure, when taken over the eastern part of the basin, is found to be highly correlated with the NAO index and with the angle of the jet stream in the western NAB. In section 3, we study the evolution of an initial, highly idealized jet stream as a function of its orientation, within a baroclinic QG model, and compare the analytical results with the observations. Section 4 summarizes the overall results of this study.

## 2. Total kinetic energy (TKE): An observational study

### a. *Geostrophic TKE index*

The TKE is used here as a daily measure of collective strength of the weather systems over the NAB. This measure is highly relevant for the study of weather and of its extremes, especially in a changing climate. We define the TKE, denoted simply by $E$, as

$$E(x,y,p,t) = u^2(x,y,p,t) + v^2(x,y,p,t), \qquad (1)$$

where $u$ and $v$ are the daily mean zonal and meridional velocities, respectively. Note that no filtering is used, and thus the TKE reflects daily variability across all time scales.

In this paper, we utilize the NCEP–NCAR reanalysis (Kalnay et al. 1996) to examine the interannual variability of the TKE. The reanalysis was used at its resolution of 2.5° latitude × 2.5° longitude over the 65-yr interval from January 1948 to December 2012.

While the actual TKE in Eq. (1) is available from the reanalysis, we found it more convenient to calculate the TKE of the geostrophic wind ($u_g$, $v_g$) from daily means of geopotential height. This choice was mainly made for consistency with previous studies of storm track variability, such as Blackmon and Lau (1980), which analyzed geopotential fields. We concentrate here on the NAB, defined as the rectangle (15°–65°N, 85°W–0°). The correlation between the average over the domain of the daily GTKE and the TKE computed from the reanalysis winds is larger than 0.93 at all the levels between the surface and 200 hPa.

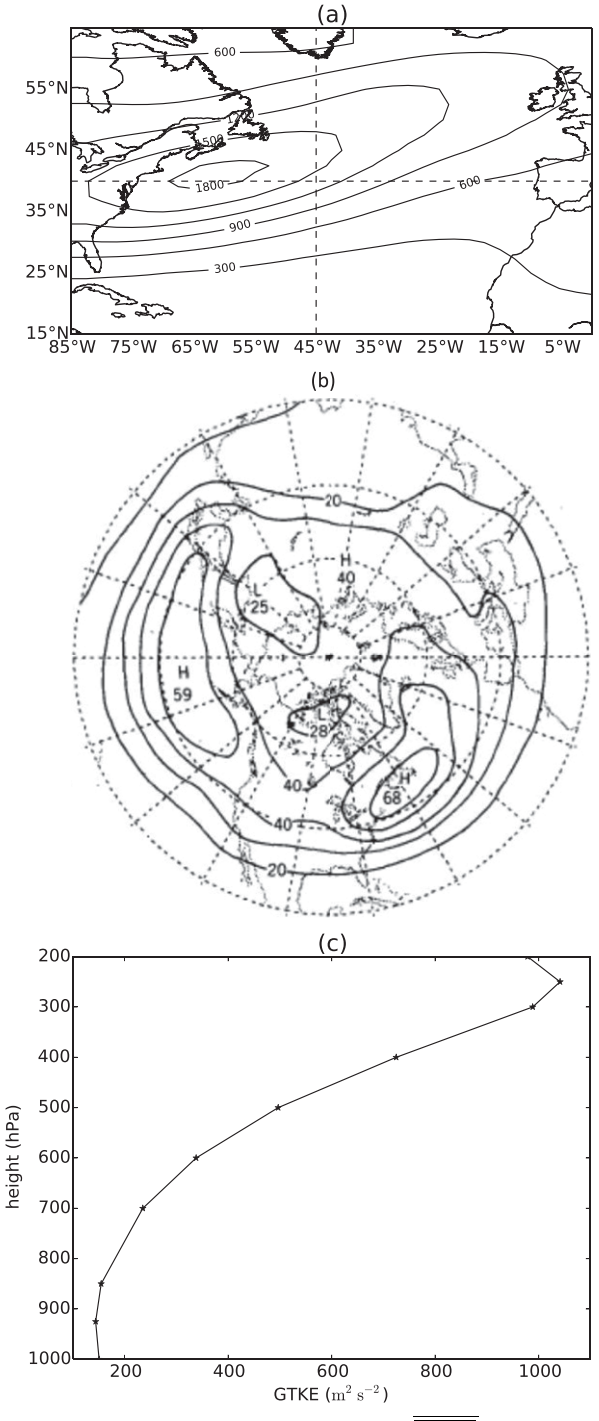


FIG. 1. The winter (DJFM) climatology of $\overline{\overline{\text{GTKE}}}$ in the NAB, defined as the (15°–65°N, 85°–0°W) rectangle. (a) The $\overline{\overline{\text{GTKE}}}$ is shown at 400 hPa, based on the NCEP–NCAR reanalysis for 1948–2012; the contour interval is 300 $\text{m}^{-2}\,\text{s}^{-2}$, with the innermost contour having a value of 1800 $\text{m}^{-2}\,\text{s}^{-2}$ and the outermost a value of 300 $\text{m}^{-2}\,\text{s}^{-2}$; the light vertical and horizontal dashed lines correspond to the 45°W meridian and the 40°N parallel, respectively, which subdivide the NAB into four quadrants. (b) Distribution of the observed root-mean-square field of 500-hPa heights, bandpass filtered in the 2.5–6-day band from Fig. 8 in Blackmon and Lau (1980); the contour interval is 10 m. (c) The vertical profile of the $\overline{\overline{\text{GTKE}}}$ spatial average ($\text{m}^2\,\text{s}^{-2}$) over the NAB, as a function of pressure level.

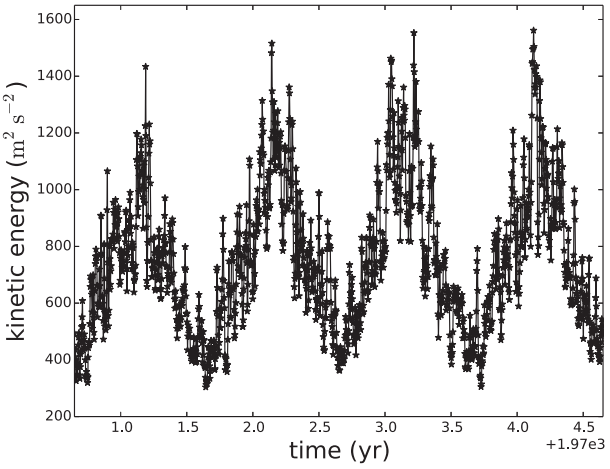


FIG. 2. The evolution in time of the spatial average $\langle\text{GTKE}\rangle$ ($\text{m}^2\,\text{s}^{-2}$) of the daily GTKE over the NAB for the 4-yr interval of 1970.5–1974.65 at 400 hPa.

The winter (DJFM) climatological average of the GTKE over the entire dataset, $\overline{\overline{\text{GTKE}}}$, is plotted in Fig. 1a, at $p = 400$ hPa. The climatological-mean structure of the GTKE is consistent with that of the standard deviation of 500-hPa geopotential height in 2.5–6-day bandpass-filtered data [cf. Fig. 1b here and Fig. 2 in Blackmon and Lau (1980)]. The climatological maximum of GTKE is found to the south of the maximum of the bandpass-filtered data, owing to the presence of the strong mean jet to the south. This consistency between Figs. 1a and 1b here confirms that the GTKE is closely related to the synoptic-scale transient eddies found along the North Atlantic storm track.

The height dependence of the $\overline{\overline{\text{GTKE}}}$, averaged over the NAB, is plotted in Fig. 1c. In the lower layers, 1000–850 hPa, the $\overline{\overline{\text{GTKE}}}$ is almost constant, probably because of high momentum mixing in the planetary boundary layer. Above 700 hPa, the $\overline{\overline{\text{GTKE}}}$ increases rapidly and reaches its maximum at 250 hPa. This increase is associated with the baroclinicity of the atmospheric eddies.

The evolution in time of the daily spatial average $\langle\text{GTKE}\rangle_{\text{NAB}}$ over the entire NAB at 400 hPa is shown in Fig. 2 for the four years 1971–74. These contiguous years exhibit substantial differences in the GTKE, and there was no discontinuity in data coverage or quality at that time (Kalnay et al. 1996). In the figure, the seasonal cycle of the GTKE is the most prominent signal. Interannual variability is also substantial, especially between the winter seasons, although the annual GTKE daily maxima are very close.

Power spectra of the daily $\langle\text{GTKE}\rangle$ time series were calculated for all 65 yr; here and elsewhere, when there is no ambiguity, we drop the NAB subscript. The four

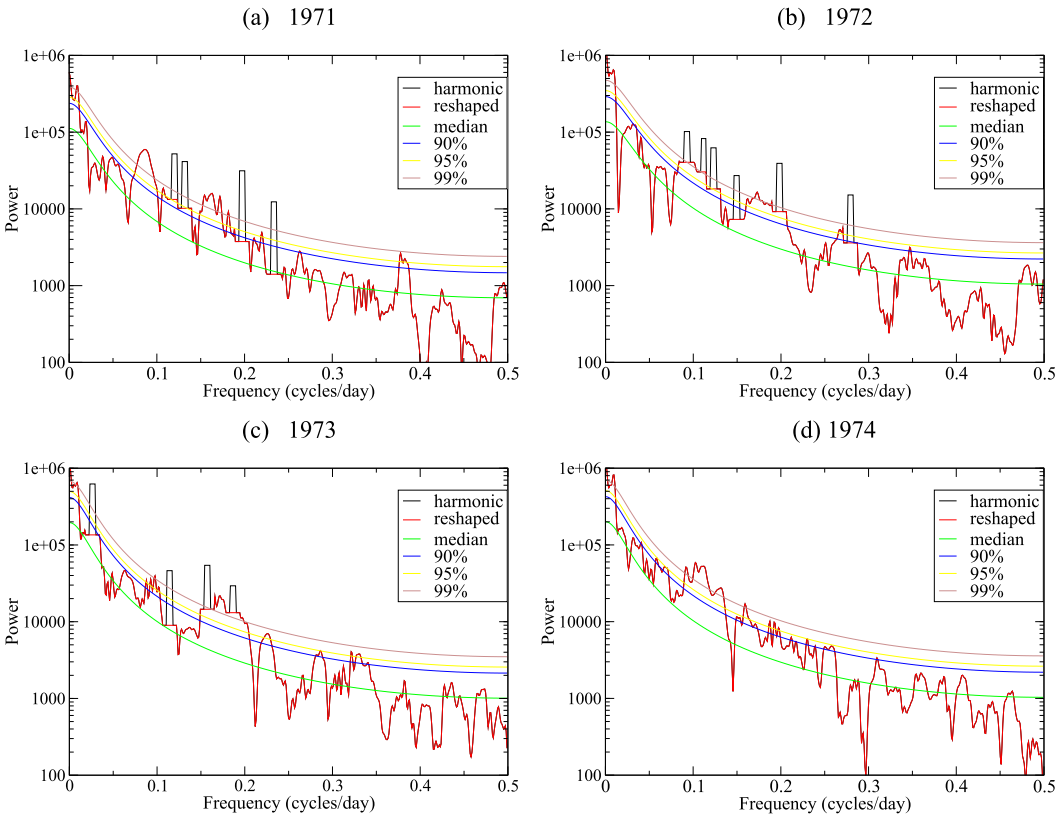


FIG. 3. The power spectrum of the daily ⟨GTKE⟩ for the four years: (a) 1971, (b) 1972, (c) 1973, and (d) 1974. The power spectrum for each year was calculated over the time interval beginning at 0.8 of the previous year and ending at 1.5 of the year indicated. The computation was done using the Mann and Lees (1996) version of the multitaper method, within the SSA-MTM Toolkit of Ghil et al. (2002); see the documentation online (http://www.atmos.ucla.edu/tcd/ssa). Three distinct estimates of the continuous background of the spectrum—harmonic (black), reshaped (red), and median (green)—are indicated in the legend of each panel, along with the confidence intervals of 90% (blue), 95% (yellow), and 99% (brown); see references for details.

successive years 1971, 1972, 1973, and 1974 are found to illustrate fairly well the differences in power spectra from one year to another and they are shown in Fig. 3. Variability in the 6–14-day band exceeds the 99% significance level in a test against red noise (Mann and Lees 1996; Ghil et al. 2002) of the multitaper method for all the years. This band includes medium-range weather forecasting time scales, as well as most persistent anomalies, such as blocking; see Ghil and Robertson (2002, and references therein), as well as Croci-Maspoli et al. (2007). There are also substantial year-to-year differences in the energy in this band, whose causes we plan to examine more closely in follow-up work.

We denote the winter average (DJFM) of the 400-hPa GTKE by $\overline{\text{GTKE}}^{(\text{DJFM})}$ and plot its spatial distribution over the entire NAB in Fig. 4 for the same four years as in Figs. 2 and 3. Our notations for spatial and temporal averages follow, roughly, the ones introduced in Lorenz (1967, chapter III).

There are significant differences between the years in the maximum value of the $\overline{\text{GTKE}}$ and in its spatial pattern; here and elsewhere we drop the superscript (DJFM) when it is clear from the context. These differences are clearly associated with year-to-year changes in the storm track. The largest value of $\overline{\text{GTKE}}$, above $2400\,\text{m}^2\,\text{s}^{-2}$, occurs in 1972, while the smallest maximum, barely above $1500\,\text{m}^2\,\text{s}^{-2}$, occurs in 1973, and the patterns are also quite different.

To gain further dynamical insight into these differences, we partitioned the NAB into four rectangular regions, divided by the 45°W meridian and the 40°N parallel. While this subdivision of the rectangular NAB domain might seem arbitrary at first sight, there were no a priori valid physical criteria for the choice of any simple subdivisions, and the results validated a posteriori our intuitive choice.

The GTKE values over the northeast (NE) and southeast (SE) quadrants are most highly correlated

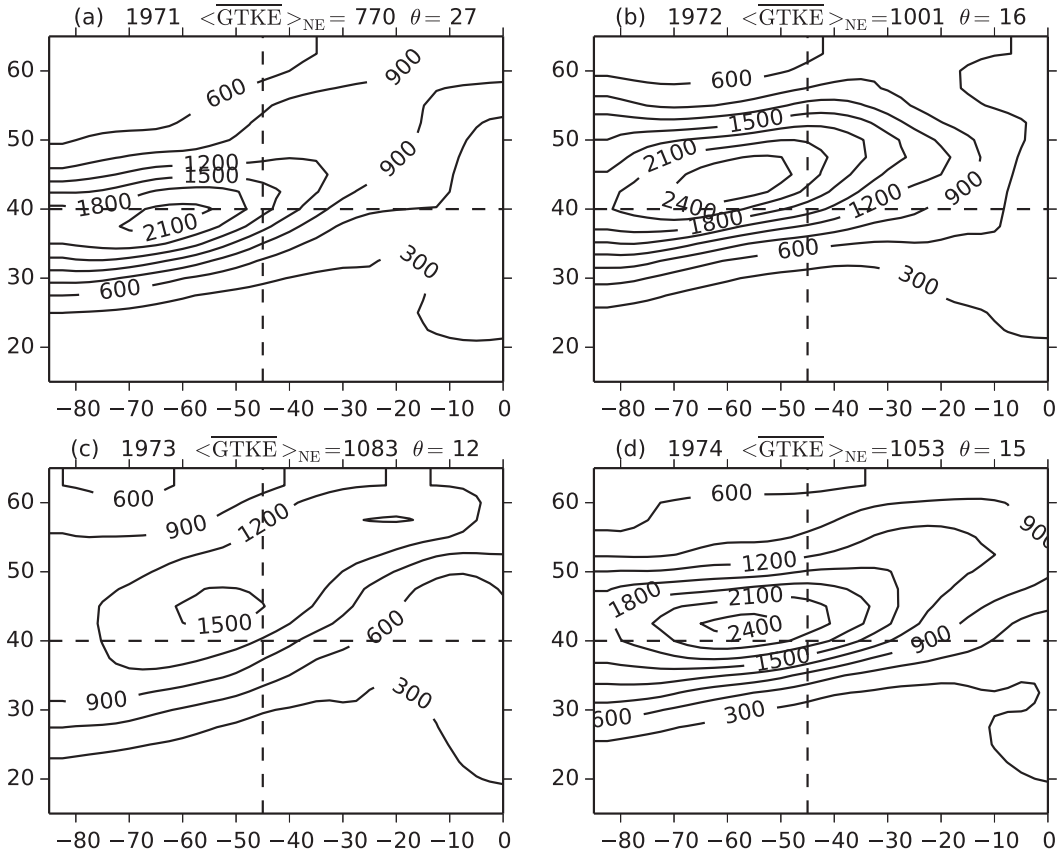


FIG. 4. The spatial distribution over the NAB of the winter (DJMF)-average $\overline{\text{GTKE}}$ at 400 hPa; contour interval is 300 $\text{m}^2\,\text{s}^{-2}$. Plots are for four selected years: (a) 1971, (b) 1972, (c) 1973, and (d) 1974. The value of $\langle\overline{\text{GTKE}}\rangle_{\text{NE}}$ ($\text{m}^2\,\text{s}^{-2}$) is given at the top of each panel along with the $\theta$ values; $\langle\overline{\text{GTKE}}\rangle_{\text{NE}}$ is the spatial average of $\overline{\text{GTKE}}$ over the NE quadrant.

with the NAO, as shown below. We also note, though, that the spatial mean $\langle\overline{\text{GTKE}}\rangle_{\text{NE}}$ over the NE Atlantic is largest in 1973, when it attains the value of 1083 $\text{m}^2\,\text{s}^{-2}$. As we shall see, what matters most to this spatial average is not the strength of the jet stream but its direction (see Figs. 11 and 9 of the present paper, and their discussion, in section 2c).

The DJFM average of the spatially averaged GTKE was then calculated for each quadrant and for each year available at different levels. Figure 5 shows standardized time series of $\langle\overline{\text{GTKE}}\rangle$ for the NE and SE quadrants at 400 hPa. Note that the mean $\langle\overline{\text{GTKE}}\rangle_{\text{NE}}$ of the time series in the NE quadrant is substantially larger than in the SE one since most of the winter storms pass through the NE quadrant. This fact is obvious from all four panels of Fig. 4, as well as from Table 1.

The relationship of the GTKE time series with the NAO was examined by using correlations between the winter average of the NAO index—denoted by NAOI in the figures—and $\langle\overline{\text{GTKE}}\rangle$ in the four quadrants. The NAO index we use is the monthly index over the years 1823–2008, as compiled by Jones et al. (1997) and plotted in Fig. 6 here. This index is the difference between the normalized sea level pressure at Gibraltar and the normalized sea level pressure over southwestern Iceland. Jones and colleagues used early instrumental data back to 1823. The dataset was modified in November 2000 and the effect of this change is most evident in the summer; see https://crudata.uea.ac.uk/~timo/datapages/naoi.htm. The four correlation values are, respectively, NE = 0.82, SE = −0.79, northwest (NW) = 0.54, and southwest (SW) = −0.56 with the largest one occurring in the NE quadrant, as expected. There is, furthermore, phase opposition between the northern and southern quadrants.

The number of winter days when the average wind speed is higher than 30 $\text{m}\,\text{s}^{-1}$ (i.e., when $\langle\text{GTKE}\rangle > 910\,\text{m}^2\,\text{s}^{-2}$) and varies between 13 and 103 days in the NE quadrant (i.e., a variation by almost a factor of 8 between winters). Both the mean and the variation in the NE quadrant are significantly larger than the range of 0–2 days in the SE quadrant. Standardized time series

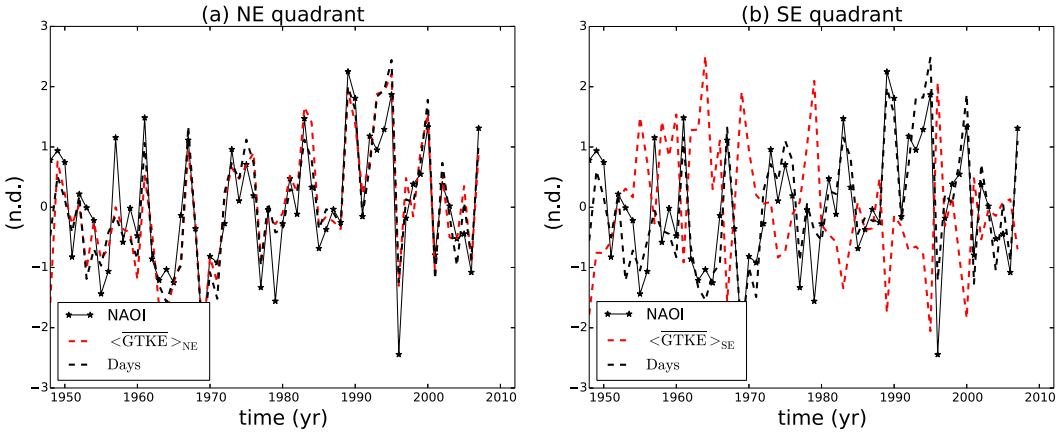


FIG. 5. The time series of the winter (DJFM)-average values—normalized by their standard deviation, given in Table 1—of the NAO index (NAOI, solid black line), $\langle\overline{\text{GTKE}}\rangle$ at 400 hPa (dashed red line), and number of days in a given winter when $\langle\overline{\text{GTKE}}\rangle > 910\,\text{m}^2\,\text{s}^{-2}$ (dashed black line); the latter is the same as the number of days when the wind speed $> 30\,\text{m}\,\text{s}^{-1}$ on average: for the (a) NE and (b) SE quadrant.

of the number of days are also shown in Fig. 5, and they are highly correlated with the NAO index in the NE quadrant. The $30\,\text{m}\,\text{s}^{-1}$ threshold was chosen to maximize this correlation, which equals 0.86, but the latter is not very sensitive to reasonable changes in the threshold.

Similar calculations were carried out for other levels in the reanalysis dataset. While the results (not shown) are similar to those reported here, the best correlations were obtained for the 400-hPa level. Hence we have concentrated on this level in the present investigation, while also reporting results for the 200-hPa level near the tropopause and the 1000-hPa level near the surface. The correlation between $\langle\text{GTKE}\rangle$ at 400 hPa and at 1000 hPa is 0.71 and the number of days when the average wind speed is higher than $19\,\text{m}\,\text{s}^{-1}$ (i.e., when $\langle\text{GTKE}\rangle$ exceeds $360\,\text{m}^2\,\text{s}^{-2}$) is 8–54 days in the NE quadrant, varying by almost a factor of 7 between winters. The $19\,\text{m}\,\text{s}^{-1}$ threshold value chosen here was used by Wang et al. (2011) to define the storminess state in the surface layer over western Europe.

We further examined the relationship between GTKE and the NAO by partitioning the 400-hPa kinetic energy into subseasonal and interannual components. The filtering was done as follows. First we computed the winter mean of the geopotential at 400 hPa for each year; these fields correspond to the interannual component of the circulation. The differences between the daily geopotential and the winter-mean fields correspond to the subseasonal perturbations of the circulation.

We then computed the geostrophic wind and the kinetic energy of each field. The kinetic energy of the winter-average geopotential is denoted by $\text{GKE}_{\text{av}}$ and the kinetic energy of the perturbations by $\text{GKE}_{\text{pert}}$. In Fig. 7, we plot the time series of the winter average over the NE quadrant for $\langle\overline{\text{GTKE}}\rangle$, $\langle\overline{\text{GKE}_{\text{av}}}\rangle$, and $\langle\overline{\text{GKE}_{\text{pert}}}\rangle$,

TABLE 1. Properties of the winter (DJFM) means of key time series in our dataset of 64 winters, 1948–2012. The $\langle\text{GTKE}\rangle$ series for the NE and SE quadrants are both given at 400 hPa.

| Time series | Mean | Std dev | Correlation |
|---|---|---|---|
| NAO index (NAOI) | 1.5 | 4.4 | +1.0 |
| $\langle\text{GTKE}\rangle_{\text{NE}}$ ($\text{m}^2\,\text{s}^{-2}$) | 998 | 17 | +0.81 |
| $\langle\text{GTKE}\rangle_{\text{SE}}$ ($\text{m}^2\,\text{s}^{-2}$) | 268 | 46 | −0.79 |
| $\langle\text{GTKE}\rangle_{\text{NE}} > 910$ ($\text{m}^2\,\text{s}^{-2}$) | 57 | 19 | +0.86 |

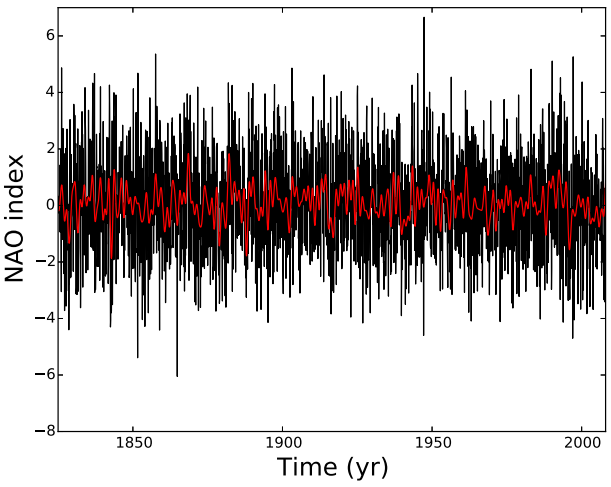


FIG. 6. The NAO index ($y$ axis from −8 to +6 in increments of 2) for the years 1823–2008 monthly average (black curve) and low-pass-filter component (red curve). The latter was obtained with a Chebyshev filter of type I, with a cutoff frequency of 0.5 cycle per year; see Feliks et al. (2013) and Table 1 therein for details.

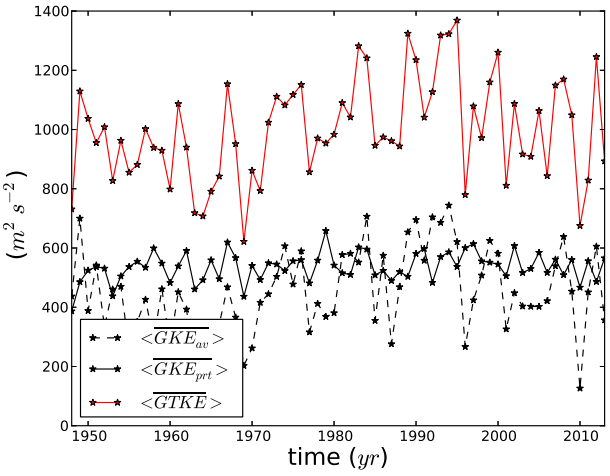


FIG. 7. The time series of the winter (DJFM) average for the NE quadrant of $\langle\overline{\text{GTKE}}\rangle$ (solid red line), $\langle\overline{\text{GKE}_{\text{av}}}\rangle$ (dotted line), and $\langle\overline{\text{GKE}_{\text{pert}}}\rangle$ (solid black line).

and several statistical properties of these energies are given in Table 2.

The total energy, $\langle\overline{\text{GTKE}}\rangle$, is 2–4 times larger than $\langle\overline{\text{GKE}_{\text{av}}}\rangle$ and about 2 times larger than $\langle\overline{\text{GKE}_{\text{pert}}}\rangle$, while $\langle\overline{\text{GKE}_{\text{pert}}}\rangle$ is larger than $\langle\overline{\text{GKE}_{\text{av}}}\rangle$. On the other hand, the variability of $\langle\overline{\text{GTKE}}\rangle$ and that of $\langle\overline{\text{GKE}_{\text{av}}}\rangle$ are much larger than that of $\langle\overline{\text{GKE}_{\text{pert}}}\rangle$. The NAO index is highly correlated with $\langle\overline{\text{GKE}_{\text{av}}}\rangle$, at 0.73, while its correlation with $\langle\overline{\text{GKE}_{\text{pert}}}\rangle$ is very low, at 0.08. We thus conclude that, in the NE quadrant, the high correlation of 0.81 between $\langle\overline{\text{GTKE}}\rangle$ and the NAO index is mainly associated with the interannual component of the circulation. On the other hand, the energy of the subseasonal transient eddies is independent of the seasonal-average NAO, as shown by the very low correlation between $\langle\overline{\text{GKE}_{\text{pert}}}\rangle$ and the NAO index.

This result is consistently found across all levels, with the correlation between the NAO index and $\langle\overline{\text{GKE}_{\text{av}}}\rangle$ being about 0.72, while the correlation with $\langle\overline{\text{GKE}_{\text{pert}}}\rangle$ is close to zero. According to these results, the intensity of the storms is affected by both low- and high-frequency components of the large-scale flows, but the interannual variability of the storms' energy is mainly determined by the low-frequency component of the flows, at least in the large NE-quadrant average considered here.

In the SE quadrant the picture is very different. The correlation between the seasonal-average NAO index and $\langle\overline{\text{GKE}_{\text{av}}}\rangle$ increases with height, reaching its negative maximum of $-0.72$ at 250 hPa, while the correlation is close to zero below 850 hPa. The correlation between the NAO index and $\langle\overline{\text{GKE}_{\text{pert}}}\rangle$, on the contrary, decreases with height, and it attains its negative maximum of $-0.66$ at 925 hPa, with the correlation being close to zero above 300 hPa. Similar behavior was found when we apply a high-pass filter to the geopotential height fields to specify the perturbation field $\langle\overline{\text{GKE}_{\text{pert}}}\rangle$, and the high-pass filter corresponds to periods shorter than 14, 21, and 28 days. But when the high-pass filter corresponds to periods shorter than 8 days, the correlation of $\langle\overline{\text{GKE}_{\text{pert}}}\rangle$ with the NAO index drops to –0.22. From the above analysis, we conclude that the energy of the subseasonal transient eddies in the SE quadrant is substantially affected by the seasonal-average NAO at altitudes below 500 hPa.

TABLE 2. Properties of the winter (DJFM) means of key time series in our dataset of 64 winters, 1948–2012, in the NE quadrant. The $\langle$GTKE$\rangle$ series are given at 400 hPa.

| Time series | Mean | Std dev | Correlation |
|---|---|---|---|
| NAO index (NAOI) | 1.5 | 4.4 | +1.0 |
| $\langle\overline{\text{GTKE}}\rangle$ ($\text{m}^2\,\text{s}^{-2}$) | 998 | 171 | +0.81 |
| $\langle\overline{\text{GKE}_{\text{av}}}\rangle$ ($\text{m}^2\,\text{s}^{-2}$) | 452 | 141 | +0.73 |
| $\langle\overline{\text{GKE}_{\text{pert}}}\rangle$ ($\text{m}^2\,\text{s}^{-2}$) | 536 | 48 | +0.08 |

### b. *Interannual oscillatory modes*

Feliks et al. (2010) have identified oscillatory modes of interannual variability in the NAO index and it is of interest here to determine whether these are present in the $\langle$GTKE$\rangle$ and, if so, whether the variability of such modes is synchronized between the two indices. The synchronization of chaotic systems, in which both the phase and amplitude of the time series produced by two such systems are required to evolve synchronously in time, is a much stronger connection than mere linear correlation; see, for instance, Boccaletti et al. (2002, and references therein).

We carried out, therefore, a synchronization analysis that follows those of Feliks et al. (2010, 2013) and of Groth and Ghil (2011). First, we examined the interannual variability of each time series separately. Because of the large seasonal and intraseasonal variability, we remove all subannual frequencies with a low-pass filter prior to spectral analysis. The choice of the filter is critical in order to avoid aliasing effects as a result of the severe subsampling associated with the 64 yearly values retained in the subsequent analysis. An inappropriately chosen low-pass filter may not only alter the amplitude of the oscillations but may even lead to spurious interannual oscillations in the annually subsampled time series. Specifically, annual sampling of winter seasonal averages from a monthly time series of the NAO index will cause aliasing in the interannual oscillations (Gray and Madden 1986; Madden and Jones 2001; Feliks et al. 2013).

To remove the strong seasonal cycle in the $\langle$GTKE$\rangle$, we first calculated monthly averages from the daily

values. To the monthly time series so obtained, we then applied a 12-month moving-average filter. Next, we derived annually sampled time series by simply taking all January values from this smoothed time series and checked that the results below are almost the same when taking another month. The preprocessing was the same for the NAO, except that for its index we had to start with the monthly values.

Singular-spectrum analysis [SSA: Ghil et al. (2002, and references therein)] was then applied to each of these time series to isolate the interannual oscillatory components whose synchronicity between ⟨GTKE⟩ and the NAO we wish to test. The statistical significance of the oscillatory modes was assessed by means of Monte Carlo SSA (MC-SSA: Allen and Smith 1996), with an ensemble size of 100 surrogate time series. To check the robustness of the peaks identified via SSA, we applied the Mann and Lees (1996) version of the multitaper method (MTM), with three tapers; see also Ghil et al. (2002) and the documentation available at http://www.atmos.ucla.edu/tcd/ssa. As for SSA, we assessed the statistical significance of the MTM results against a red-noise null hypothesis.

The SSA was applied with a window width $M$ of 30 yr. The pair (1, 2) of temporal empirical orthogonal functions (T-EOFs) captures the lowest-frequency components—that is, those with periods longer than $M$—including a nonlinear trend (Ghil et al. 2002). We then removed this long-term trend, as captured by the pair (1, 2) of reconstructed components (RCs).

To isolate any underlying low-frequency oscillations, we applied SSA to the detrended indices with the same window width. A summary of the modes identified at a 95% level of significance in both MC-SSA and MTM are given in Table 3, along with the percentage of variance captured by the corresponding SSA mode. The ⟨GTKE⟩ variability in the NE quadrant contains three significant oscillatory modes, with periods of 8.7, 4.8, and 2.6 yr. These oscillatory modes are close in period to the interannual oscillations found previously in the NAO index (Feliks et al. 2010, 2013).

We then applied a bivariate version of multichannel SSA (MSSA: Keppenne and Ghil 1993; Plaut and Vautard 1994; Ghil et al. 2002) to the preprocessed $\langle \mathrm{GTKE} \rangle_{\mathrm{NE}}$ as channel 1 and to the preprocessed NAO index as channel 2, with the same window width of $M$ = 30 yr and normalizing each channel by its respective variance. The spatiotemporal–EOF (ST–EOF) pair (1, 2) still captures the lowest-frequency components, including the nonlinear trend, in both channels, and we removed this long-term trend, as captured by the ST–RC pair (1, 2) of the MSSA analysis, where ST–RCs denote the spatiotemporal RCs in MSSA (Plaut and Vautard 1994; Ghil et al. 2002).

TABLE 3. Oscillatory modes in the $\langle \mathrm{GTKE} \rangle_{\mathrm{NE}}$ that are statistically significant at the 95% significance level in both the SSA and MTM analyses. The third column gives the percentage of variance captured by the corresponding mode; for the three periodicities in rows 2–4, the variance is given as a percentage of the variance of the time series after having subtracted the trend in row 1; that is, the percentage of total variance is 0.71 times the entry in the table.

| T-EOF | Period (yr) | Variance (%) | |
|---|---|---|---|
| (1, 2) | Trend | 29 | |
| (1, 2) | 8.7 | 17 | (detrended) |
| (3, 4) | 2.6 | 15 | (detrended) |
| (5, 6) | 4.8 | 13 | (detrended) |

Next, we proceeded as for the single-channel SSA above and applied MSSA to the pair of detrended indices above, with the same window width. The signals that were found to be significant at the two-sided 95% level are analyzed further below. These ST–RC pairs have periods of 2.8 yr (pair 1–2, with 19% of the variance) and 8.5 yr (pair 3–4, with 15% of the variance).

Figure 8a shows that the interannual oscillatory modes of the ⟨GTKE⟩ in the NE quadrant and those of the NAO index are completely synchronized in the 8–9-yr band. The other two oscillatory modes, at 2–3 and 4–5 yr, are also found to be completely synchronized (not shown).

To summarize, most of the weather activity in the eastern part of the NAB is located in its NE quadrant, as revealed by the strong ⟨GTKE⟩ there. Furthermore, the interannual variability of $\langle \mathrm{GTKE} \rangle_{\mathrm{NE}}$ and that of the NAO closely track each other.

We have also calculated the correlation between $\langle \mathrm{GTKE} \rangle_{\mathrm{NE}}$ and Hurrell North Atlantic Oscillation (NAO) index (PC based). This index is the principal component (PC) of the leading EOF in the usual, purely spatial decomposition of the sea level pressure anomalies over the Atlantic rectangular domain (20°–80°N, 90°W–40°E). The correlation in this case is 0.88 for $\langle \mathrm{GTKE} \rangle_{\mathrm{NE}}$ at 400 hPa and 0.89 at 500 hPa. These high correlations raise the possibility that ⟨GTKE⟩ in the NE quadrant of our NAB domain could be used as an alternative to the NAO index to measure, and possibly even predict, atmospheric activity in the eastern North Atlantic and over parts of western Europe; the simplicity of calculating $\langle \mathrm{GTKE} \rangle_{\mathrm{NE}}$ versus the current, instrumental NAO index is a definite advantage of the former.

### c. *Variations in jet stream diffluence*

We next examine the connection between the diffluence of the jet stream over the North Atlantic, the $\langle \mathrm{GTKE} \rangle_{\mathrm{NE}}$, and the NAO. The diffluence angle of the jet stream at a given point is defined as the angle between the tangent to the streakline at that point and the

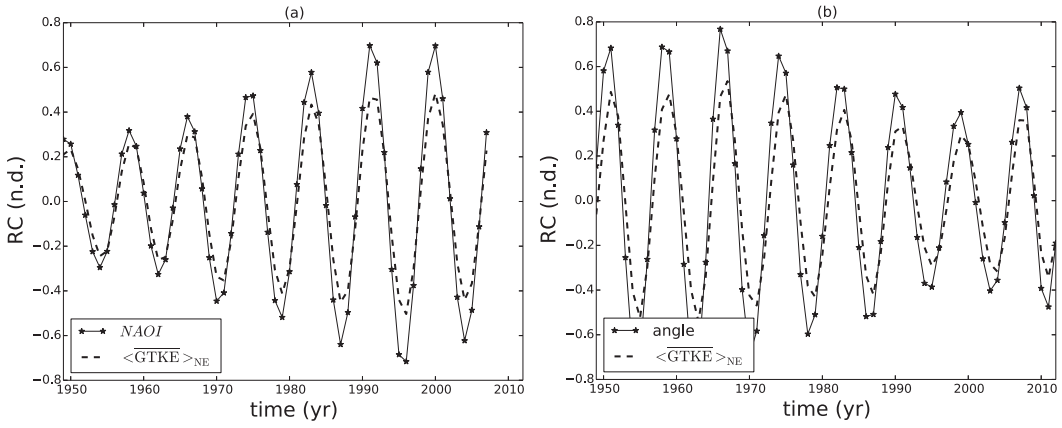


FIG. 8. Synchronization of $\langle\overline{\text{GTKE}}\rangle_{\text{NE}}$ with the NAO index and the diffluence angle of the jet. (a) The RC corresponding to the 8.5-yr oscillatory mode in the NAO index (solid line) and in the $\langle\overline{\text{GTKE}}\rangle_{\text{NE}}$ (dashed line). (b) The RC of the winter 8.6-yr oscillatory mode in the diffluence angle at 200 hPa (solid line) and $\langle\overline{\text{GTKE}}\rangle_{\text{NE}}$ at 400 hPa (dashed line).

latitude circle through it, minus the climatological-mean angle of the jet stream axis at a reference point or over a reference segment.

The eddies that develop along the jet stream owing to its instability are advected eastward by the mean jet; their number and strength are a function of this instability. It appears that there are no studies so far that explicitly address the baroclinic instability of the jet stream as a function of its diffluence. This instability is the subject of section 3 in the present paper.

We first examine here the connection between the diffluence angle of the mean jet stream and $\langle\text{GTKE}\rangle$ over the North Atlantic's NE quadrant. The reference segment chosen here for this purpose is (40°N, 75°–80°W). The corresponding climatological mean angle is 1.6°; that is, the jet stream at 40°N is almost zonal, and it reaches its maximum speed there. Since this angle is almost zero, we consider below the diffluence angle at a point with respect to the latitude circle at that point; see Fig. 9. We further define the diffluence over a region as the spatial average of the jet stream diffluence angle over that region and seek the spatial domain for which the correlation between the diffluence angle over it and $\langle\text{GTKE}\rangle_{\text{NE}}$ is maximized.

Table 4 gives this maximization result for three distinct levels—200, 400, and 1000 hPa—in terms of the maximizing region, its diffluence angle, and the correlation between the two time series—angle and $\langle\text{GTKE}\rangle_{\text{NE}}$ —taken over the 65 yr of the dataset, 1948–2012. The region that maximizes the correlation can turn out to be a rectangle in spherical coordinates or just a segment of a parallel or a meridian, depending on the level and on the correlation being maximized in absolute value.

The mean diffluence angle at the two upper levels, 200 and 400 hPa, is positive (i.e., the flow is southwesterly) and it exhibits small interannual changes, while at the lower level (1000 hPa) the diffluence angle is negative; that is, the flow is northwesterly and confluent with respect to the zonal flow. Table 4 shows that the correlation-maximizing regions are geographically close at all levels and that all three lie in the northern part of the NW quadrant, given by 50°–60°N, 70°–45°W. The regions where interannual variations in the jet's diffluence angle correlate most closely with those of $\langle\text{GTKE}\rangle_{\text{NE}}$ are thus located north of the mean axis of the jet (cf. Fig. 1a); see also Fig. 9 for the location of the region at 200 hPa.

The striking phase difference in mean diffluence angle between the upper and the lower levels can be explained by the baroclinic development associated with the Gulf Stream's SST front, as suggested by the modeling results in section 3a below. The strongest correlation between $\langle\text{GTKE}\rangle_{\text{NE}}$ and the diffluence angle equals −0.76, and it occurs at 200 hPa. Figure 10 shows the time series of the

TABLE 4. The regions of the NE Atlantic that optimize the correlation between their diffluence angle and $\langle\text{GTKE}\rangle_{\text{NE}}$ at different levels. The columns give the coordinates of the region and the corresponding mean angle of diffluence (in degrees with respect to the zonal direction), its standard deviation (SD), and its correlation with $\langle\text{GTKE}\rangle_{\text{NE}}$ at 400 hPa over the entire time interval 1948–2012.

| Level (hPa) | Coordinates | Mean (°) | SD (°) | Corr. |
|---|---|---|---|---|
| 200 | 55°N, 67.5°–45°W | +18 | 6 | +0.76 |
| 400 | 55°–57.5°N, 62.5°W | +16 | 9 | −0.67 |
| 1000 | 52.5°–60.0°N, 62.5°–45°W | −13 | 9 | −0.67 |

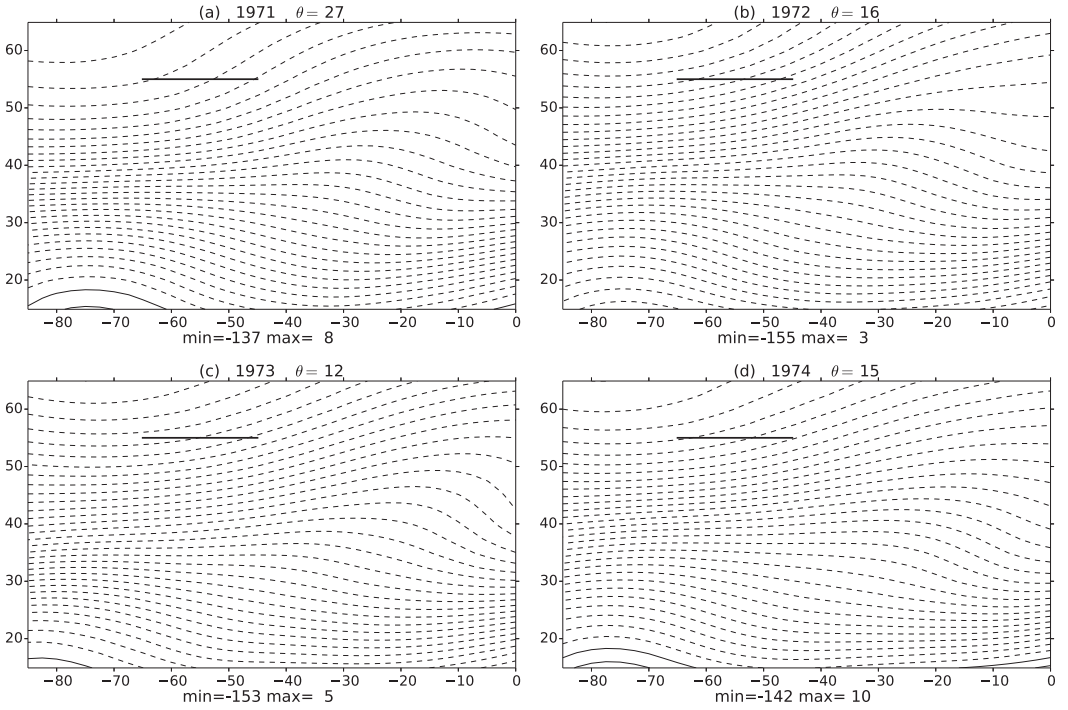


FIG. 9. The mean winter streamfunction ($10^{-6}\,m^2\,s^{-1}$) in the NAB at 200 hPa for the years: (a) 1971, (b) 1972, (c) 1973, and (d) 1974. The contour interval is $5 \times 10^{-6}\,m^2\,s^{-2}$, while the solid and dashed lines correspond to positive and negative values, respectively. The mean jet stream diffluence is computed with respect to the heavy horizontal zonal line shown here in the NW quadrant of each panel; and the mean angle $\theta$ of the streamfunction across this straight line is given at the top of each panel.

diffluence angle for the correlation-optimizing region, over the time interval 1948–2012; the angle varies between 5° and 35°.

The negative correlation between $\langle \mathrm{GTKE} \rangle_{\mathrm{NE}}$ and the diffluence angle of the optimizing region indicates that, when the jet stream is more zonal and less diffluent, the eddies in the NE quadrant are stronger; see also Fig. 11. We find that $\langle \mathrm{GTKE} \rangle_{\mathrm{NE}}$ is mostly influenced by the diffluence angle rather than by the strength of the jet stream. This is seen, for example, by reexamining Fig. 4 for the years 1971–74: the maximum value of $\overline{\mathrm{GTKE}}^{(\mathrm{DJFM})}$ over the entire NAB in 1973 is significantly smaller than in the other years but in the NE quadrant $\langle \mathrm{GTKE} \rangle$ is the largest (cf. the caption of Fig. 4c). At the same time, the diffluence angle in the optimizing region, within the NW quadrant, is smaller in 1973 than in the other three years, as seen from Fig. 9. Thus, small changes of 5°–10° in the jet stream angle in the optimizing region can be accompanied by large changes in $\langle \mathrm{GTKE} \rangle_{\mathrm{NE}}$.

To find the interannual variability of the jet stream diffluence angle in the optimizing region, we first low-pass filtered the variability by retaining periods that are shorter than 1 yr; this was done by applying a 12-month running average to the monthly mean streamfunction at 200 hPa. Then we derived a subsampled time series by taking all the January streamfunction fields; the results below are almost the same when taking another month (not shown).

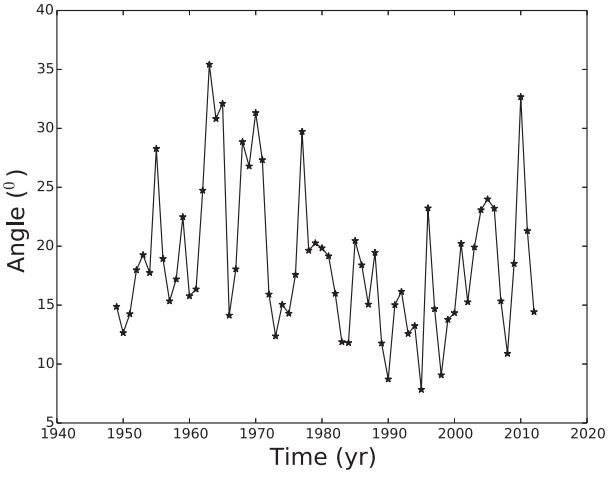


FIG. 10. The time evolution of the diffluence angle of the jet axis in the correlation-optimizing region at altitude 200 hPa; see text and Figs. 5 and 8 for details on the optimization.

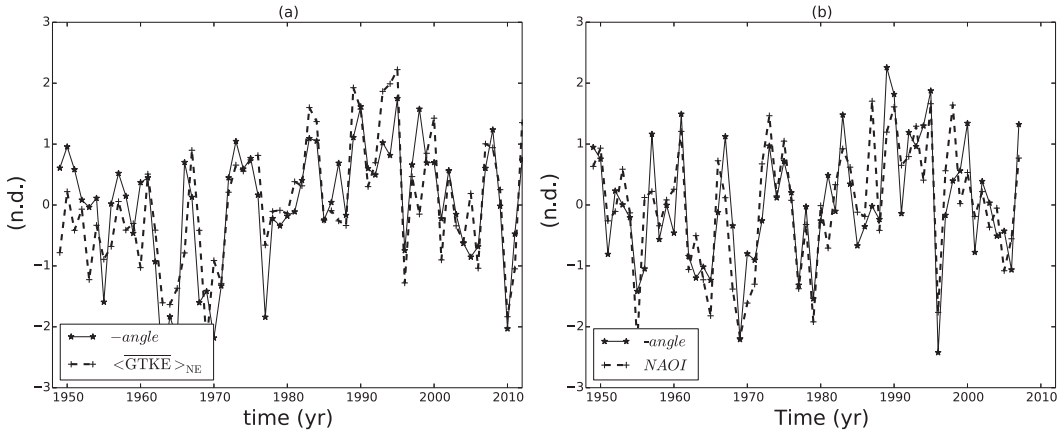


FIG. 11. The diffluence angle (multiplied by −1) of the jet stream in the optimizing region (solid line in both panels): (a) vs $\langle\overline{\text{GTKE}}\rangle_{\text{NE}}$ at 400 hPa (dashed line); (b) vs the NAO index (dashed line). The values are normalized by the standard deviation after subtracting the mean.

From the 64 January streamfunction fields so obtained, we calculated the corresponding diffluence angles, and then we followed the procedure described in section 2b above; that is, SSA was applied to the annual time series of the angles, with a window width of $M = 30$ yr. The T–EOF pair (1, 2) captures the lowest-frequency components, including the nonlinear trend, and it contains 28% of the variance. The second pair (3, 4) has a period of 8.2 yr and it captures 20% of the variance.

We then applied a bivariate MSSA to the $\langle\text{GTKE}\rangle_{\text{NE}}$ (channel 1) and to the optimized orientation angle at 200 hPa (channel 2), with the same window width of 30 yr, and normalizing each channel by its respective variance. In this case, it was not even necessary to remove the trend, since it was small enough and did not mask the oscillatory modes in the significance test. The ST–EOF pair (1, 2) captures the lowest-frequency components, including the nonlinear trend in both channels.

Next, we applied MSSA to the detrended indices with the same window width and found two ST–EOF pairs that are statistically significant at the two-sided 95% level: pair (1, 2) has a period of 8.4 yr and it captures 21% of the variance, while pair (3, 4) has a period of 4.8 yr and captures 15% of the variance. Both oscillatory modes are completely synchronized (cf. Fig. 8b).

We have also sought the regions that optimize the correlation between their mean diffluence angle and the NAO index. The results, at the same three levels as in Table 4, are now given in Table 5. The maximum correlation is −0.8 for the jet at 400 hPa. There is thus also a close connection between the angle of the jet stream in the NW quadrant and the NAO index. The optimizing regions and their diffluence angles are fairly similar, whether the optimization is done with respect to the NAO index or with respect to $\langle\overline{\text{GTKE}}\rangle_{\text{NE}}$, as can be seen by comparing Tables 4 and 5. This similarity is consistent with the close relationship between the NAO index and $\langle\overline{\text{GTKE}}\rangle_{\text{NE}}$ (cf. Figs. 5 and 8).

In summary, we have shown that interannual variability in the total kinetic energy of the North Atlantic's NE quadrant, $\langle\overline{\text{GTKE}}\rangle_{\text{NE}}$, is closely related to the diffluence angle of the jet stream in its NW quadrant. In the next section we use a quasigeostrophic, baroclinic model to gain insight into the dynamics of this relationship.

## 3. Atmospheric jet dynamics in the presence of an SST front

Most previous studies of baroclinic or barotropic instability of a westerly jet have been restricted to purely zonal flows. Some stability analyses have considered a tilted flow in which the speed alone changes with height. Miles (1964) and Robinson and McWilliams (1974), for instance, studied the stability of such a height-dependent flow and found that the fastest-growing unstable wave propagates parallel to the mean flow. On the other hand, Grotjahn (1981) and Pedlosky (1982) showed that, for such a flow, the most unstable wave does not necessarily propagate parallel to the mean flow: its growth rate, phase speed, and wave pattern change dramatically with different orientations of the mean flow.

TABLE 5. As in Table 4, but optimizing the correlation between the region's diffluence angle and the NAO index.

| Level (hPa) | Coordinates | Mean (°) | SD (°) | Corr. |
|---|---|---|---|---|
| 200 | 52.5°–60°N, 75°–52.5°W | +14 | 6 | −0.78 |
| 400 | 55°N, 72.5°–52.5°W | +14 | 7 | −0.80 |
| 1000 | 52.5°–60°N, 62.5°–45°W | −13 | 9 | −0.65 |

### a. A QG tilted-jet model with no forcing

Stimulated by the observational findings in the previous section 2c, we study here some dynamical aspects of a jet that is initially tilted with respect to the zonal direction. Our study relies on the nonlinear, baroclinic QG model of Feliks et al. (2007). This model consists of the standard potential vorticity equation (Pedlosky 1982; Holton and Hakim 2012) and it uses a vertical decomposition in terms of the barotropic and first baroclinic normal modes (Flierl 1978; Feliks 1990).

In the present context, it is helpful to write the QG potential vorticity equation in a coordinate frame $(x_r, y_r)$ that is rotated by an angle $\theta$ with respect to the zonal direction. The equation for the modal amplitudes (Flierl 1978) is

$$\frac{\partial q_m}{\partial t} + \beta\left(\cos\theta\frac{\partial \psi_m}{\partial x_r} + \sin\theta\frac{\partial \psi_m}{\partial y_r}\right) + \sum_{ij}\xi_{ijm}J(\psi_i, q_j) = r_H\nabla^4\psi_m - \frac{H}{H_a}\phi_m(0)w_a(z=0), \tag{2}$$

where the Jacobian $J$ and the Laplacian $\nabla^2$, and hence also the biharmonic operator $\nabla^4$, in the rotated coordinate frame have the same form as in the nonrotated system. Note that the angle $\theta$ only enters this equation by modifying the $\beta$ term. As in Feliks et al. (2007), we retain only the two lowest modes, $m = 0, 1$, and use

$$q_m = \nabla^2\psi_m - \lambda^2\psi_m, \quad \xi_{ijm} = \int \phi_i\phi_j\phi_m\, dz. \tag{3}$$

The triple interaction coefficients $\xi_{ijm}$ are all equal to zero or one, except $\xi_{111}$. The lower-boundary condition for the free atmosphere at $z = 0$ above an ocean surface is

$$\frac{H}{H_a}\frac{\partial}{\partial t}\left[\frac{\partial}{\partial z}\left(\frac{1}{S}\frac{\partial \psi}{\partial z}\right)\right] = \frac{H}{H_a}w_a(x, y, z=0, t) = \gamma\nabla^2\psi, \tag{4}$$

where the nondimensional constant

$$\gamma = \frac{1}{2\pi}\frac{H_E f L}{H_a V} \tag{5}$$

determines the strength of the ocean-surface friction. Here $\gamma$ is given in terms of the mechanical component of the vertical velocity at the top of a marine atmospheric boundary layer (MABL) of depth $H_E$ (cf. Feliks et al. 2004), $H_a$ is the height of the free atmosphere, $L$ is the horizontal length scale across the front, and $V$ scales the wind speed in the cross-front direction, which in turn is proportional to the inverse of the frontal Rossby number. Numerical values of the model parameters for the simulations are given in Table 6.

TABLE 6. Characteristic scales and reference values for the atmospheric model.

| | |
|---|---|
| $L$ (km) | 50 |
| $H$ (km) | 10 |
| $H_a$ (km) | 10 |
| $H_E$ (km) | 0.8 |
| $T_i$ (day) | 0.58 |
| $V$ (m s$^{-1}$) | 1 |
| $\beta_0$ (m$^{-1}$ s$^{-1}$) | $1.8 \times 10^{-11}$ |
| $f$ (s$^{-1}$) | $10^{-4}$ |
| $\theta_0$ (K) | 300 |
| $L/\lambda_1$ (km) | 575 |
| $g$ (m s$^{-2}$) | 9.81 |

The initial state in this study is an atmospheric jet flowing parallel to the $x_r$ axis. The boundary conditions on the boundaries normal to the $x_r$ axis are periodic, and they are zero on the boundaries normal to the $x_r$ axis. The streamfunction at any height $z$ is given by

$$\psi(z) = \psi_{\mathrm{BT}} + \phi_1(z)\psi_{\mathrm{BC}}; \tag{6}$$

here $\phi_1(z)$ is the vertical structure of the first baroclinic mode, denoted by (BC), while $\phi_1(0) = 0.7$ corresponds to the surface $z = 0$, which is at the top of the MABL, and $\phi_1(H) = -2.3$ corresponds to the top of the free atmosphere, which is at an altitude of 200 hPa.

The numerical scheme is as in Feliks (1990) and Feliks et al. (2004, 2007). Key features include fourth-order accurate discretization by finite elements in the horizontal (cf. Haidvogel et al. 1980) and a second-order Adams–Bashforth scheme in time.

The initial jet, parallel to the $x_r$ axis, has the following structure:

$$\psi_{\mathrm{BT}}(y_r) = A\,\mathrm{erf}\left(\frac{y_c}{y_{\mathrm{jet}}}\right),$$
$$\psi_{\mathrm{BC}}(y_r) = -\frac{A}{\phi_1(0)}\,\mathrm{erf}\left(\frac{y_c}{y_{\mathrm{jet}}}\right), \tag{7}$$

where $A = 55$ and $y_{\mathrm{jet}} = 200\,\mathrm{km}/L$. This jet is at rest at $z = 0$ and it has a maximum speed of $(28\,\mathrm{m\,s^{-1}})/V$ at the top of the free atmosphere, $z = H$. The grid interval is $50\,\mathrm{km}/L = 1$ and the domain has $170 \times 100$ grid points. Thus the domain, in dimensional units, is an 8500 km $\times$ 5000 km rectangle, rotated by $\theta$ degrees with respect to the zonal direction, and all the integrations are 30 days long in dimensional units.

The evolution of the initial jet as a function of the orientation angle $\theta$ is shown in Fig. 12. Note that the maps in this figure are all plotted in the rotated $(x_r, y_r)$ frame. For $\theta = 0°$, the initial jet persists at its initial latitude until the end of the integration, while unstable

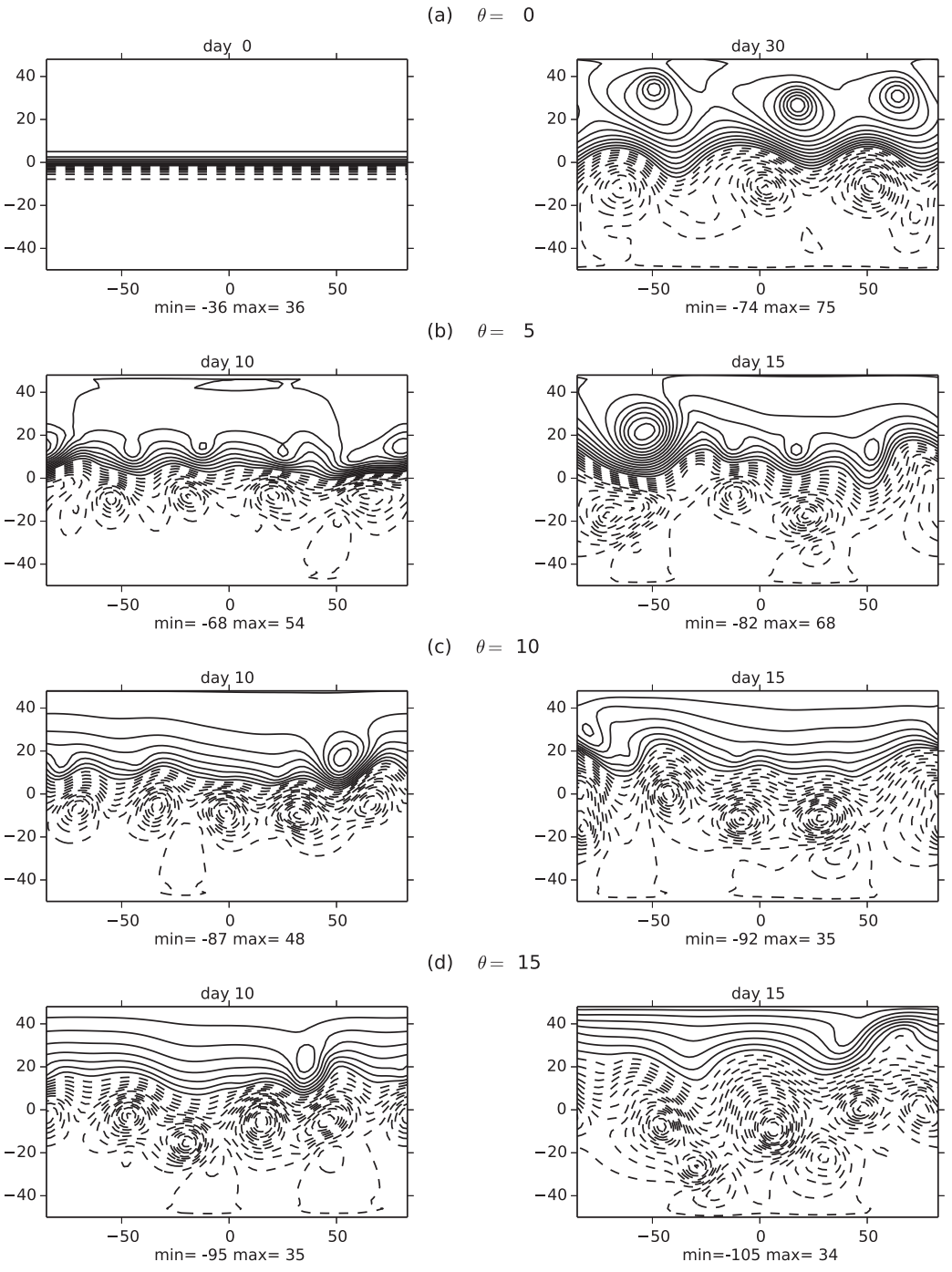


FIG. 12. The evolution of the baroclinic mode streamfunction for several orientation angles $\theta$ : (a) 0°, (b) 5°, (c) 10°, and (d) 15°. (top left) The initial state for all four experiments is the same ($\theta = 0°$, day 0). All spatial patterns are shown for the same rectangular domain of $8500/L$ km $\times$ $5000/L$ km. The scaling of the axes in this figure is in nondimensional units; these units have to be multiplied by 50 km to yield dimensional distances. Solid (dashed) lines correspond to positive (negative) values.

waves do grow on it. By day 30, the most unstable wave dominates the flow and its wavelength is about 1750 km.

For $\theta > 0$, we observe a northward propagation of the jet and the unstable waves propagate along the jet axis. Both the propagation speed and the growth rate of the most unstable wave increase as the jet orientation angle increases. In the barotropic mode (not shown), the propagation of the jet along the $y_r$ direction—perpendicular

to the jet axis $x_r$—is faster than that of the baroclinic mode and, after several days, the barotropic jet structure collapses.

The increase in the growth rate of the most unstable mode with $\theta$ is consistent, over all, with the previous results of Grotjahn (1981) and Pedlosky (1982). From Fig. 12, we can estimate the propagation speed of the jet along the $y_r$ axis: for $\theta = 5°$ this speed equals about 50 km day$^{-1}$, while for $\theta = 10°$ it is between 50 and 65 km day$^{-1}$, and for $\theta = 15°$ it is 75–100 km day$^{-1}$.

The northward propagation of the oriented jet (more precisely along the $y_r$ axis) is explained by the group velocity of a packet, in our case the packet is the jet given in Eq. (7). For a given Rossby wave, with zonal and meridional wavenumbers $k$ and $l$, the group velocity $C_g^y$ along the $y$ axis (Pedlosky 1982) is

$$C_g^y = 2\frac{\beta kl}{(k^2 + l^2 + \lambda^2)^2}. \tag{8}$$

For $\theta = 0$, the flow is zonal (i.e., along the $x$ axis); thus $\psi$ is constant, and hence $k = 0$. It follows from Eq. (8) that $C_g^y = 0$, so the jet does not propagate northward and persist in its initial place till the end of the integration. In the rotated $(x_r, y_r)$ coordinate frame, the Fourier components of the initial jet have a wavenumber $l_r \neq 0$ along the $y_r$ axis, while $k_r = 0$ along the $x_r$ axis. The $l_r$ wavenumber projected onto the unrotated $(x, y)$ coordinate frame has two components, $k = l_r \sin\theta$ and $l = l_r \cos\theta$:

$$C_g^y = 2\frac{\beta l_r^2 \cos\theta \sin\theta}{(l_r^2 + \lambda^2)^2}. \tag{9}$$

Previous stability studies of an oriented flow found no propagation of the initial flow, since in these studies the flow was a function of height $z$ only and so the group velocity of the initial packet is always zero.

Values of $\theta > 0$ imply that $C_g^y > 0$ and hence the initial packet propagates northward, while for $\theta < 0$ and thus $C_g^y < 0$, the packet propagates southward. As the magnitude $|\theta|$ of the orientation angle increases, the group velocity increases. This explains the numerically observed faster northward propagation of the jet in its initial stages. The slower propagation of the baroclinic part of the jet, relative to the barotropic part, can also be explained by the group velocity. The denominator of the right-hand side of Eq. (9) for the barotropic mode is $l_r^2$, while for the baroclinic component it is $l_r^2 + \lambda_1^2$; here $\lambda_1$ is smaller than $l_r$ but still significant, so the group velocity of the barotropic mode is larger than that of the baroclinic mode.

From the above arguments and the simulations in Fig. 12 we conclude that only a purely zonal jet can persist at its initial latitude, while any tilted initial jet will propagate in an approximately meridional direction in the absence of any forcing. This raises the question of how the observed mean seasonal jet stream—which has an average angle of about 14° in the NW quadrant, as seen in Fig. 9—can remain approximately stationary over an entire season, rather than propagate away and disappear poleward. Next we show that, by adding a forcing to the atmospheric model, a tilted jet can persist near its initial position.

### b. *Steady-state solution forced by an SST front*

In this subsection, we study a steady-state solution of the two-mode QG model of Eq. (2) in the presence of a tilted SST front analogous to the Gulf Stream near the Grand Banks region. Therefore, we examine first the nature of this front in the observations based on the Simple Ocean Data Assimilation (SODA) data, 1958–2007 (Carton and Giese 2008). In Figs. 13c,d, the front is shown for the years 1971 and 1975, while the corresponding mean winter streamfunction field in the NW quadrant is shown in Figs. 13a,b.

We focus on the features of the strongest front that lies within the correlation-optimizing region of the jet stream at 200 hPa or close to this region. The optimizing region is defined in Table 4 and outlined in Figs. 13a–d as a heavy straight line: the strongest front lies within the red box in Figs. 13c,d. The influence of such a front on the atmospheric flow above the NAB and downstream of it was studied by Feliks et al. (2011).

Here we gather preliminary evidence for the hypothesis that the orientation and strength of this front in the winter affect the strength and the diffluence of the atmospheric jet in the NAB's NW quadrant. First, we examine the influence of the SST front orientation on the jet stream diffluence. The mean strength of this SST front is about 2.1 K/50 km for each of the two years in Figs. 13c,d, but its angle $\theta$, defined as the angle between the tangent to the isotherm and a latitude circle, does change from year to year: in 1971 the slope of the front was −54° and in 1975 it was −73°, while the diffluence angle of the jet stream was 27° in 1971 and 14° in 1975 (cf. Figs. 13a and 13b).

We found a similarly strong dependence of jet stream diffluence on SST front angle for other pairs of years for which the SST front had approximately the same strength. In the years when the front orientation was closest to −45°, the jet stream diffluence was largest (not shown).

Next, we examine the influence of the SST front strength on the jet stream diffluence when the angle of the front is approximately constant. For instance, in the years 1971 and 1982 the change in the orientation of the SST front was less than 1°. But the absolute value of

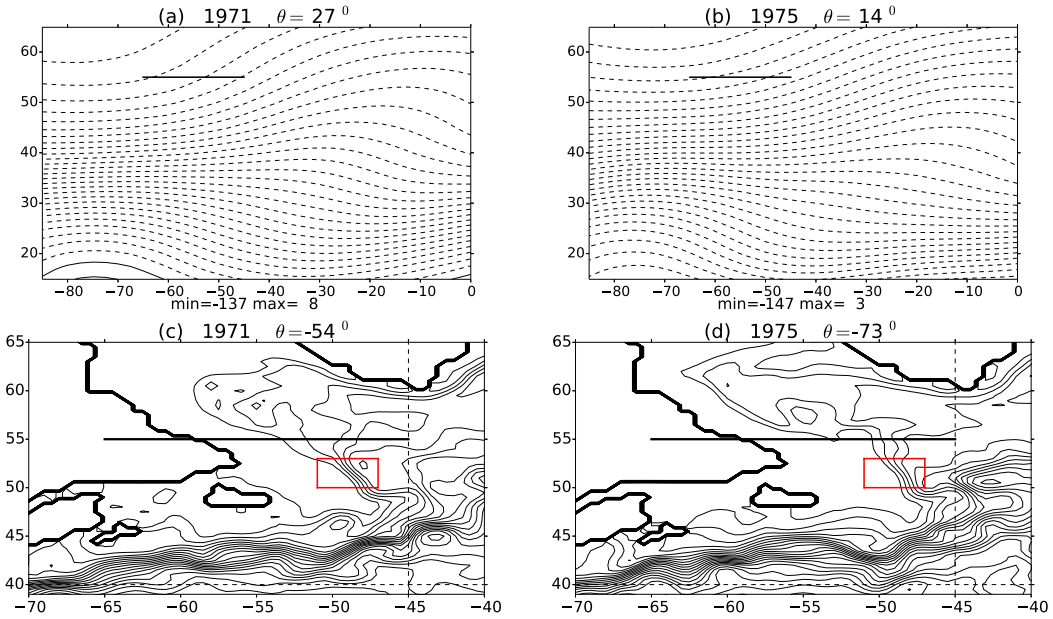


FIG. 13. The effect of the SST front angle on the jet stream angle. (a),(b) Mean winter streamlines at 200 hPa for 1971 with $\theta = 27°$ and 1975 with 14°, respectively; see Fig. 9 for details. (c),(d) The mean winter sea surface temperature (SST) field (°C), in the NAB from the SODA data for the same years but with $\theta = -54°$ and $-73°$, respectively. The heavy horizontal zonal line in the NW quadrant here is the same as in (a),(b) and it is given in Table 4 for the 200-hPa level. The contour interval is 1°C and the contours have been smoothed by applying a three-point smoothing operator along the $x$ and $y$ axes, with weights (0.25, 0.5, 0.25); this recursive filter is equivalent to a nine-point smoother with the weights (1/16, 1/8, 1/16, 1/8, 1/4, 1/8, 1/16, 1/8, 1/16). The red box indicates the region where the tilted SST front is identified in the text.

the SST gradient in 1971 was 2.1 K/50 km and the jet stream diffluence was 27°, while in 1982 the SST gradient was about 1.4 K/50 km and the jet stream diffluence was 16°. Thus we suspect that larger SST front gradients contribute to larger jet stream diffluence, and this hypothesis is supported by other pairs of years in which large changes in the SST front gradient occur while its orientation was fairly similar (not shown).

These effects of both SST front strength and orientation on the jet stream lead us to define the Gulf Stream gradient angle (GSGA) index that takes into account both the strength and the angle of the SST front. We define this GSGA index to be

$$\text{GSGA} = \sin[(\text{mean angle of the front}) \times (\text{mean gradient of the front})]. \quad (10)$$

The region of highest correlation, namely 0.60, between GSGA and 200-hPa jet stream diffluence angle (as defined in Table 4) is located in the spherical rectangle (50°–53°N, 51°–47°W), plotted as the red rectangle in Figs. 13c,d. Figure 14 shows standardized time series of GSGA and the jet stream diffluence angle at 400 hPa. When the gradient in GSGA calculated over the larger domain (48°–53°N, 52°–47°W), the correlation between GSGA and jet stream diffluence angle increases even further, to 0.62. The close relation between the GSGA index defined in Eq. (10) above and jet stream diffluence strengthens our argument that both the SST front's orientation and its strength determine the atmospheric jet's diffluence. The simultaneous correlation is 3 times larger than at any lag/lead.

Interannual changes of the SST front are likely to be due to internal ocean dynamics rather than to the direct influence of the jet stream at the sea surface for the following two reasons. 1) We examined the fine structure of the SST front from the surface to a depth of 250 m in the rectangular area of interest and found it to persist at all these depths, well below the oceanic Ekman layer. 2) The scale of the jet streamflow is on the order of a thousand kilometers, while the SST front's scale is only about 50–100 km. Thus, a decisive influence of the atmospheric, synoptic-scale flow is not compatible with the strong gradient found in the SST front over a distance of 50–100 km.

These preliminary observational findings suggest the need for a systematic study of the role of the SST front orientation and gradient in determining the atmospheric

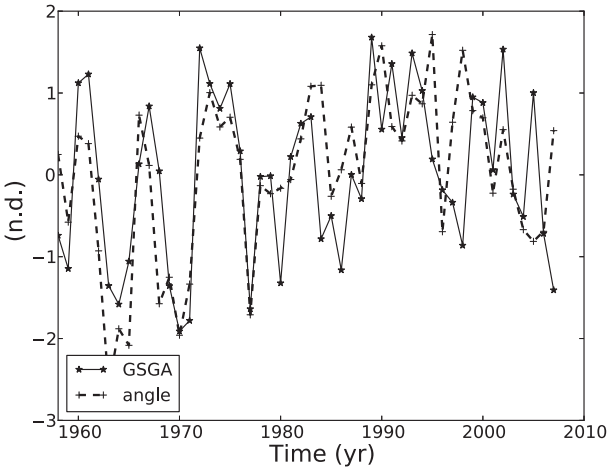


FIG. 14. The time series of the winter (DJFM) average for the GSGA index (solid line) and diffluence angle of the jet stream (broken line). The values are normalized by the standard deviation after subtracting the mean.

jet's diffluence angle. A step in this direction is taken here by studying the effects of tilting a jet away from the zonal direction.

Following Feliks et al. (2004, 2007), the vertical velocity $w_a$ at the top of the MABL over an oceanic front is given by

$$\frac{H}{H_a} w_a(x, y, z = 0, t) = \gamma \nabla^2 \psi - \alpha \nabla^2 T, \tag{11}$$

where $\gamma$ was defined in Eq. (5), while $\alpha$ is given by

$$\alpha = \frac{1}{2\pi}\left(1 - \frac{1}{2\pi}\right)\frac{gH_E^2 T^*}{H_a V^2 \theta_0}. \tag{12}$$

Feliks et al. (2004) showed that, in midlatitudes, the vertical velocity $w_a$ has two components: one due to the geostrophic flow above the MABL, which these authors called the mechanical component, and the other due to the wind induced in the MABL by the oceanic thermal front, which they called the thermal component. It is the thermal component that was considered in the tropical atmosphere by Lindzen and Nigam (1987), while the mechanical component is negligible in the tropics and was introduced into the midlatitude atmosphere–ocean coupling problem by Feliks et al. (2004, 2007). In this subsection, we examine a steady-state solution to the QG potential vorticity equation, in which the thermal field used in Eq. (11) above approximates the thermal front off the Grand Banks.

According to Eq. (12), the thermal component of $w_a$ is proportional to $H_E^2$ and $T^*$, where the (nondimensional) temperature $T$ scales like the oceanic frontal strength $T^*$. The constants $\alpha$ and $\gamma$ determine the relative importance of the near-surface flow forcing by the MABL below and the QG dynamics above, respectively. Since $\alpha$ is proportional to the strength $T^*$ of the SST front, stronger SST fronts induce stronger atmospheric circulations. The steady state Eq. (2), in the presence of an SST front, reduces to

$$\begin{aligned}\beta\frac{\partial\psi_0}{\partial x} &= -\gamma[\nabla^2\psi_0 + \phi_1(0)\nabla^2\psi_1] + \alpha\nabla^2 T,\\ \beta\frac{\partial\psi_1}{\partial x} &= \phi_1(0)\{-\gamma[\nabla^2\psi_0 + \phi_1(0)\nabla^2\psi_1] + \alpha\nabla^2 T\}.\end{aligned} \tag{13}$$

The solution to the homogeneous version of the above equations, with $\nabla^2 T = 0$, is a zonal jet stream, as shown in the previous subsection. The solution to the nonhomogeneous equations is found by writing the two-equation system (13) in a rotated coordinate frame ($x_r$, $y_r$) and assuming that a steady flow is induced in the MABL by an oriented oceanic front of infinite extent in the $\pm x_r$ directions. For such a front, all the SST contour lines are parallel to the $x_r$ axis.

The nonhomogeneous equations with such an SST front in the rotated coordinate frame are

$$\begin{aligned}b\frac{\partial\psi_0}{\partial y_r} &= -\gamma\left[\frac{\partial^2\psi_0}{\partial y_r^2} + \phi_1(0)\frac{\partial^2\psi_1}{\partial y_r^2}\right] + \alpha\frac{\partial^2 T}{\partial y_r^2},\\ b\frac{\partial\psi_1}{\partial y_r} &= \phi_1(0)\left\{-\gamma\left[\frac{\partial^2\psi_0}{\partial y_r^2} + \phi_1(0)\frac{\partial^2\psi_1}{\partial y_r^2}\right] + \alpha\frac{\partial^2 T}{\partial y_r^2}\right\},\end{aligned} \tag{14}$$

where $b = \beta\sin(\theta)$. Dividing the second equation by $\phi_1(0)$ and subtracting it from the first equation, we get

$$\psi_1 = \phi_1(0)\psi_0. \tag{15}$$

Substituting $\psi_1$ in the first equation of Eq. (14), we are left with only one equation to solve:

$$b\frac{\partial\psi_0}{\partial y_r} = -\gamma_1\frac{\partial^2\psi_0}{\partial y_r^2} + \alpha\frac{\partial^2 T}{\partial y_r^2}, \tag{16}$$

where $\gamma_1 = \gamma[1 + \phi_1^2(0)]$.

When the SST front is given by $T = -T^*\,\mathrm{erf}(y_r/y_0)$, the solution to Eq. (16) is

$$\begin{aligned}\psi_0(y_r) = \frac{\alpha}{\gamma_1}\exp\left(\frac{b^2 y_0^2}{4\gamma_1^2} - \frac{by_r}{\gamma_1}\right)\mathrm{erf}\left(\frac{by_0}{2\gamma_1} - \frac{y_r}{y_0}\right)\\ + k_1\exp\left(-\frac{by_r}{\gamma_1}\right) + k_2.\end{aligned} \tag{17}$$

Since $\psi_0 \to 0$ as $y_r \to \pm\infty$, it follows that $k_2 = 0$ and $k_1 = -(\alpha/\gamma_1)\exp(b^2 y_0^2/4\gamma_1^2)$. This solution is plotted in Fig. 15 as a function of the orientation angle $\theta$. The nonhomogeneous part of the solution has a sharp gradient above the SST front and is zero to the southeast of it, for $y_r < 0$, while the solution decays slowly to the

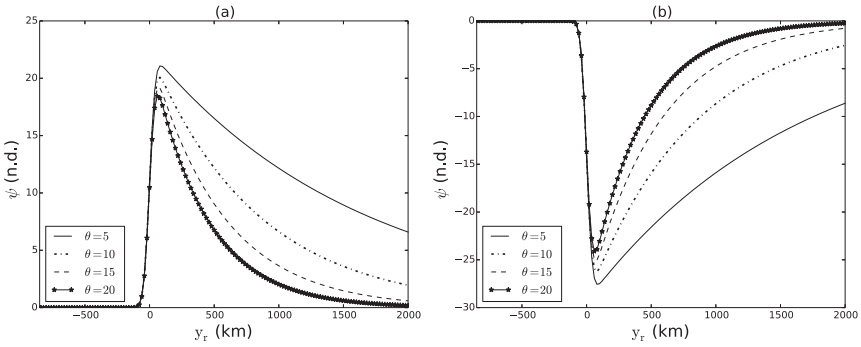


FIG. 15. The analytic solution of the nonhomogeneous part of $\psi$ as a function of $y_r$, the distance from the SST front: (a) at 200 and (b) at 1000 hPa. The distance on the abscissa is from the antisymmetry axis of the SST front at $y_r = 0$ km. The different curves correspond to different diffluence angles $\theta$ : 5°(solid), 10° (dashed–dotted), 15° (dashed), and 20° (solid with star symbols).

northwest of the front. The distinct curves for $\theta = 5°, 10°, 15°$, and 20° of arc show that the decay rate increases with the orientation angle $\theta$ of the front. If the angle $\theta$ is negative, the analytical solution is a mirror image of the one in the figure; that is, $\psi(y_r; -\theta) = \psi(-y_r; \theta)$.

The solution at 200 hPa for a positive (i.e., poleward) tilt of the Gulf Stream front near the Grand Banks, as plotted in Fig. 15a, tends to turn the jet northward, as described by Eq. (17). Thus, the total flow aloft has a southerly component; that is, the flow is toward the northeast, as observed in the NAB's NW quadrant; see again Fig. 9.

The analytical solution at 1000 hPa (Fig. 15b) rotates the flow toward the south, giving the total flow near the surface a northerly component. This northerly component near the surface is also seen over the NW quadrant in the reanalysis streamfunction maps in Fig. 16. The effect of the SST front on the overlying atmospheric circulation—via the nonhomogeneous solution to the potential vorticity equation discussed in this subsection—can thus explain the observed height-dependent correlation results in Tables 4 and 5 and the baroclinicity that these results imply.

## 4. Summary and conclusions

### *a. Summary*

The amplitude of interannual variability in the atmospheric circulation over the North Atlantic is small when compared to the amplitudes of midlatitude weather systems, like the winter cyclones, and of the intraseasonal variability [Ghil and Robertson (2002) and references therein]. It is thus not clear how this relatively weak interannual variability may affect the higher-frequency variability, including the statistics of the weather systems. We have explored here this problem using the NCEP–NCAR reanalysis for the 65 yr of 1948–2012.

The collective strength of weather systems and subseasonal variability was quantified in terms of the total kinetic energy, GTKE, calculated on a daily basis over the North Atlantic basin (NAB), given by (15°–65°N, 85°W–0°); see Fig. 1. The spatial average of GTKE over the NAB exhibits strong seasonal and subseasonal variability: the strongest variance is found between 6 and 14 days, while the weather systems, whose time scale is about 2–6 days, have less energy (Fig. 3). These results are consistent with previous studies of high- and bandpass-filtered geopotential height variance [e.g., with Blackmon et al. (1984)]. The largest GTKE values are found in the winter, and our study concentrated on the 120-day December–March season.

The spatial distribution of winter-average GTKE over the NAB shows significant year-to-year changes in strength and pattern. To analyze this variability, the NAB was partitioned into four rectangular regions, divided by the 45°W meridian and the 40°N parallel; see Figs. 1 and 4.

The correlation coefficients $r$ between the winter average of the NAO index, plotted in Fig. 6, and the seasonal and spatial average of the GTKE in the four quadrants are $r_{NE} = 0.82$, $r_{SE} = 0.79$, $r_{NW} = 0.54$ and $r_{SW} = -0.56$ Thus, the GTKE values over the NE and SE quadrants are most highly correlated with the NAO, while the GTKE magnitude in the NE quadrant is larger by an order of magnitude than in the SE quadrant; the latter difference between the GTKE magnitudes in the two quadrants is associated with the SW–NE orientation of the storm track (cf. Table 1 and Fig. 4). The very high correlations, of $r \simeq 0.8$ in absolute value, are novel, to the best of the authors' knowledge. Further work is required to fully attribute this NAO association with GTKE to

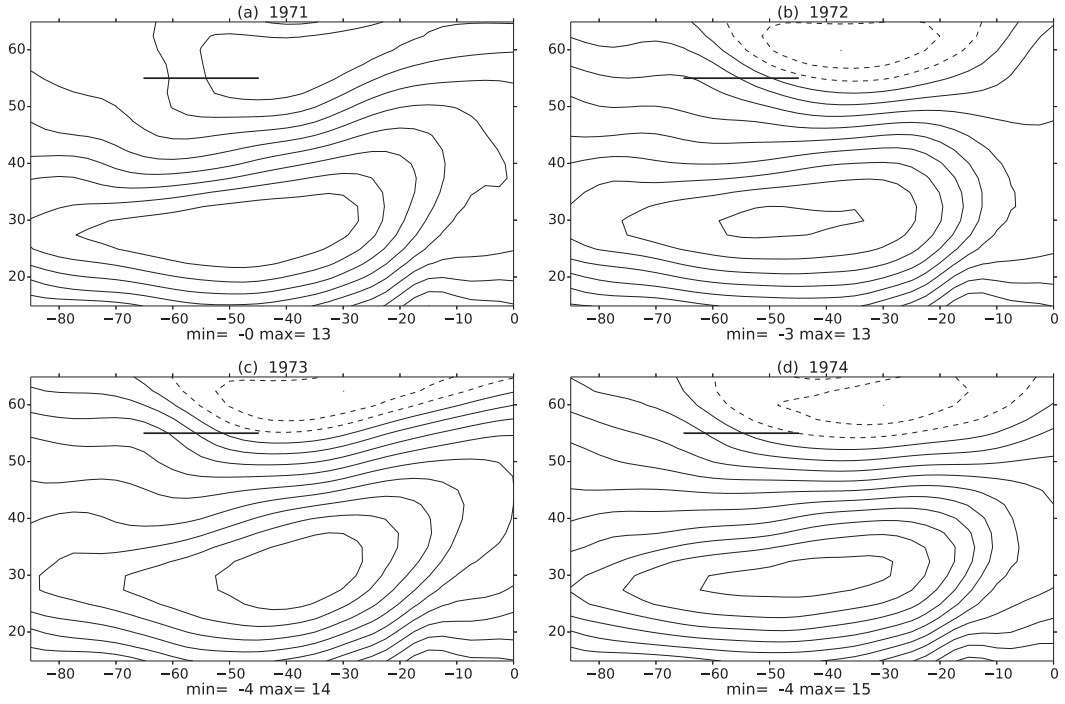


FIG. 16. The mean winter streamfunction in the NAB at 1000 hPa for the four winters of (a) 1971, (b) 1972, (c) 1973, and (d) 1974. The straight horizontal zonal line in the NW quadrant is the correlation-optimizing region where the jet stream diffluence at 200 hPa is considered in this paper. The flow across this zonal line is to the SE; that is, it is deflected southward near the surface, rather than northward, as shown for 200 hPa in Fig. 9. The contour interval is $1.5 \times 10^{-6}\,m^2\,s^{-1}$ with solid (dashed) for positive (negative) values and with min and max values given below each panel.

interannual variations in transient baroclinic wave activity, as found by Robertson and Metz (1989), versus variations in the seasonal-average circulation, as was found to be the case here.

The ⟨GTKE⟩ index provides an easily computed measure related to storminess. Thus the number of stormy days, defined as days when the average wind speed at 1000 hPa is higher than $19\,m\,s^{-1}$ (Wang et al. 2011) (i.e., when ⟨GTKE⟩ exceeds $360\,m^2\,s^{-2}$) is 8–54 days in the NE quadrant, varying by almost a factor of 7 between winters. This result has potential applications to climate prediction of the risk of storm damage and wind-energy generation.

The GTKE in the NE quadrant of the NAB (see Figs. 1 and 4) is correlated with both the NAO index and the mean orientation angle of the jet stream in the NW quadrant; see Tables 4 and 5, as well as Figs. 5–11. The correlations between the mean orientation angle and the GTKE over the NE quadrant, on the one hand, as well as between this angle and the NAO index, on the other, were all of 0.65 or higher in absolute value, when using winds at 200, 400, and 1000 hPa; see again Tables 4 and 5, as well as Fig. 8.

Only during winter does the average speed of the jet at 400 hPa in the NE quadrant exceed $30\,m\,s^{-1}$; this value corresponds roughly to the presence of a strong winter storm within the quadrant. The number of winter days with average wind speed higher than this threshold is 13–103 days in the NE quadrant (Wang et al. 2011), and it is significantly larger than the corresponding 0–2 days in the SE one; see Fig. 5.

This number of days is highly correlated with the NAO index in the NE quadrant, with $r = 0.86$. Similar calculations were carried out for other levels in the reanalysis dataset, and the results (not shown) are similar to those at 400 hPa. Since the best correlations were obtained for the 400-hPa level, we concentrated on this level in reporting the results of the present investigation, while also including results for the 200-hPa level, near the tropopause, and the 1000-hPa level, near the surface.

We note that the 400-hPa level is higher than the 700-hPa level chosen by J. Namias and colleagues at the U.S. National Weather Service in their empirical long-range weather forecasts (Namias 1968). But their team focused on forecasting large-scale, smooth flow patterns—associated these days with low-frequency, intraseasonal variability [Ghil and Robertson (2002) and references therein]—and looked for a level at which surface forcing, at or near 1000 hPa, and upper-air barotropic effects, at or

near 500 hPa, would have comparable effects. The present study, though, focuses on the low-frequency variability of actual weather, which is not as influenced by local surface forcing, although it does seem to be affected substantially by upstream, oceanic effects.

The interannual variability of GTKE over the NE quadrant was shown to contain three oscillatory modes, with periods of 8.7, 4.8, and 2.6 yr (Table 3). These oscillatory modes are highly significant statistically and close in period to the interannual oscillations found previously in the NAO index (Feliks et al. 2010, 2013). The interannual oscillatory modes of the seasonal averages $\langle \overline{\mathrm{GTKE}}_{\mathrm{NE}} \rangle$ over the NE quadrant and those of the NAO index were found to be completely synchronized and almost independent of the season (Fig. 3). The presence of these NAO-related periodicities in the GTKE provides more direct evidence of systematic interannual-to-decadal modulation of weather over the NE Atlantic.

The winter average $\langle \overline{\mathrm{GTKE}}_{\mathrm{NE}} \rangle$ was shown to be negatively and strongly correlated with the diffluence angle $\theta$ of the jet stream in the NW quadrant (Fig. 11a); this angle measures the northward tilt of the jet stream axis, away from the zonal direction. The maximum anticorrelation of $r = -0.76$ was obtained at 200 hPa, across the straight-line segment (55°N, 67.5°–45°W) (cf. Table 4); this segment is located to the north of the axis of the jet, indicating a diffluence as well as a northward tilt of the jet (cf. Fig. 9). Small changes, of 5°−10° in $\theta$, suffice to cause large changes in $\langle \overline{\mathrm{GTKE}}_{\mathrm{NE}} \rangle$. The jet stream angle correlates just as strongly with the NAO index, with $r = -0.78$ (cf. Table 5 and Fig. 11b).

Thus, a northward-tilted and more-diffluent jet is associated with the less-energetic daily weather over the NE Atlantic and Europe. This finding is consistent with previous studies of blocking and weather types over the NAB (Robertson and Metz 1990). Gerber and Vallis (2009), for instance, concluded that a localized storm track appears to be a diffluent region of weak upper-level flow that forces eddies to break, thus preventing the downstream propagation of eddy energy. Our finding on the effects of northward tilt on the storm track is also consistent with the cyclone tracking and clustering study of Gaffney et al. (2007), where one of the three clusters of wintertime cyclones over the North Atlantic was made up of northward-oriented tracks over the western part of the basin, coexisting with blocking over the NE quadrant.

To gain insight into the relation between the orientation angle of the jet stream and its downstream impact, we used the nonlinear QG baroclinic model in a $\beta$ channel of Feliks et al. (2007). A purely zonal jet was shown to persist at its initial latitude until the end of a 30-day integration. However, as the angle $\theta$ between the jet axis and the zonal direction increases, one finds that the jet loses its stability and propagates northward.

This meridional propagation is explained in terms of group velocity of a packet of Rossby waves; see section 3 and Fig. 12. For a zonal flow, the northward component $C_g^y$ of the group velocity is zero and the jet persists at its initial latitude. When the orientation angle $\theta$ is positive, $C_g^y > 0$ and the jet propagates northward, while $\theta < 0°$ yields $C_g^y < 0$ and the jet propagates southward.

It thus appears that nonzonal jets, like the North Atlantic jet stream, whose mean orientation angle is $\theta \simeq 15°$ in the upper troposphere (see Tables 4 and 5) need forcing to persist at a given latitude for more than a few days. We propose, following Feliks et al. (2004, 2007, 2011) and Brachet et al. (2012), that fairly small-scale SST fronts in the NAB supply the external forcing that maintains the nonzonal atmospheric jet over the NW Atlantic. The annual-mean orientation angle of the SST front off the Grand Banks is about −60°.

An index of Gulf Stream front orientation and amplitude over the Labrador Current region was constructed and shown to be highly correlated with 200-hPa jet diffluence to the north (Fig. 14). Together with the analytical model result, this provides further evidence that frontal SST gradients can impact of the diffluence angle of the upper-tropospheric jet, which in turn modulates the GTKE and storminess downstream over the NE Atlantic on interannual time scales.

### b. Discussion

Our highly "local" interpretation of the oceanic mechanism giving rise to a rectilinear tilted jet over the NAB is distinct from and probably complementary to the global picture of planetary-scale climatological stationary waves, whose Rossby wave dynamics was elucidated from the 1940s to the 1980s. Classical studies showed that these quasi-stationary waves were maintained by a combination of topographic and thermal forcing; see Held (1983, and references therein). Several recent studies (Brayshaw et al. 2008; Nakamura et al. 2008; Woollings et al. 2010b; Liu et al. 2013) have also considered the influence of a large-scale SST front on the tilted storm track across the NAB. These planetary- and basin-scale pictures emphasize the remote influence of zonal asymmetries in Northern Hemisphere topography and thermal forcing—like the Rockies, Himalayas, and land–ocean contrasts—or that of large-scale fronts, while our rectilinear, tilted-jet model highlights the potential role of regional, fairly small-scale thermal and mechanical driving by an SST front.

We solved analytically the steady-state problem of an atmospheric jet forced by an oriented SST front. The

analytical solution is the sum of two components: 1) the solution to the homogeneous equation, which is a zonal jet, and 2) the solution to the nonhomogeneous equation. The SST forcing tends to turn the jet northward in the upper layers, while in the lower layers the forcing tends to turn it southward.

These tendencies are observed in NCEP–NCAR reanalysis data at 200 and 1000 hPa in the NW quadrant, mainly north of the Gulf Stream SST front near the Grand Banks, as shown in Figs. 9 and 16, and they are illustrated schematically in Fig. 17. Considering the fact that the jet is nearly zonal at some level in the lower troposphere, its backing at 200 hPa, above this level, and its veering at 1000 hPa, below it, are both consistent with thermal wind balance.

A thread of literature (Jiang et al. 1995; Speich et al. 1995; Simonnet et al. 2005; Dijkstra and Ghil 2005) had argued for some time that the interannual variation in the double-gyre circulation and in its central eastward jet are due to intrinsic ocean dynamics. Furthermore, Feliks et al. (2004, 2007) have provided a mechanism, verified by Brachet et al. (2012) among others, for such an eastward jet to affect substantially the intensity and orientation of the atmospheric jet above. It appears, in fact, that the mechanical component of the mechanism by which a midlatitude SST front of even modest size affects the atmosphere is much more efficient than the thermal component.

The present paper raises the possibility that the orientation angle and thermal gradient of the SST front off the Grand Banks is a cause of the observed interannual variability of the jet stream diffluence angle in the NW quadrant of the North Atlantic. Feliks et al. (2011) have shown that the atmospheric circulation over the NAB, induced by the SST fronts off Cape Hatteras and off the Grand Banks (see Fig. 1 there) can explain the interannual variability of the NAO. Since the strength of GTKE in the NE quadrant is mainly determined by the mean angle and diffluence of the jet stream in the NW quadrant, variations in the North Atlantic's SST fronts may influence the strength of the winter storms in the eastern North Atlantic and over parts of western Europe. A study along these lines is now underway.

*Acknowledgments.* It is a pleasure to acknowledge stimulating conversations with Yochanan Kushnir. This work was supported by NSF Grant OCE-1243175 and by ONR's Multidisciplinary University Research Initiative (MURI) Grant N00014-12-1-0911. The NCEP–NCAR Reanalysis and Simple Ocean Data Assimilation (SODA) data (Version 2.0.2-4) were obtained via the IRI Climate Data Library (http://iridl.ldeo.columbia.edu). The Hurrell NAO index can be obtained online (https://climatedataguide.ucar.edu/climate-data/hurrell-northatlantic-oscillation-nao-index-pc-based).

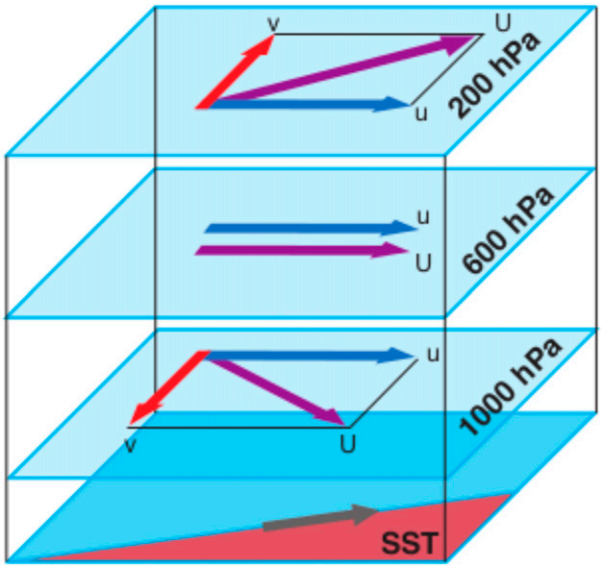


FIG. 17. Schematic diagram of the effect of a nonzonal SST front on the atmospheric jet aloft. The Gulf Stream–like SST front at the surface separates equatorward warm waters from poleward cold waters. The homogeneous, free solution is shown in blue and labeled *u*; the effect of the forcing by the thermal front is shown in red and labeled *v*, with the resultant of *u* and *v* shown in purple and labeled *U*. Note the difference in the SST front effect, and hence the resultant flow, in the upper and lower troposphere.

## REFERENCES

Allen, M. R., and L. A. Smith, 1996: Monte Carlo SSA: Detecting irregular oscillations in the presence of colored noise. *J. Climate*, **9**, 3373–3404, doi:10.1175/1520-0442(1996)009<3373:MCSDIO>2.0.CO;2.

Barnston, A. G., and R. E. Livezey, 1987: Classification, seasonality and persistence of low-frequency atmospheric circulation patterns. *Mon. Wea. Rev.*, **115**, 1083–1126, doi:10.1175/1520-0493(1987)115<1083:CSAPOL>2.0.CO;2.

Blackmon, M. L., 1976: A climatological spectral study of the 500 mb geopotential height of the Northern Hemisphere. *J. Atmos. Sci.*, **33**, 1607–1623, doi:10.1175/1520-0469(1976)033<1607:ACSSOT>2.0.CO;2.

——, and N.-C. Lau, 1980: Regional characteristics of the Northern Hemisphere wintertime circulation: A comparison of the simulation of a GFDL general circulation model with observations. *J. Atmos. Sci.*, **37**, 497–514, doi:10.1175/1520-0469(1980)037<0497:RCOTNH>2.0.CO;2.

——, Y. Lee, and J. M. Wallace, 1984: Horizontal structure of 500 mb height fluctuations with long, intermediate and short time scales. *J. Atmos. Sci.*, **41**, 961–980, doi:10.1175/1520-0469(1984)041<0961:HSOMHF>2.0.CO;2.

Boccaletti, S., J. Kurths, G. Osipov, D. L. Valladares, and C. S. Zhou, 2002: The synchronization of chaotic systems. *Phys. Rep.*, **366**, 1–2, doi:10.1016/S0370-1573(02)00137-0.

Brachet, S., F. Codron, Y. Feliks, M. Ghil, H. Le Treut, and E. Simonnet, 2012: Atmospheric circulations induced by a

midlatitude SST front: A GCM study. *J. Climate*, **25**, 1847–1853, doi:10.1175/JCLI-D-11-00329.1.

Branstator, G., 1995: Organization of storm track anomalies by recurring low-frequency circulation anomalies. *J. Atmos. Sci.*, **52**, 207–226, doi:10.1175/1520-0469(1995)052<0207:OOSTAB>2.0.CO;2.

Brayshaw, D. J., B. Hoskins, and M. Blackburn, 2008: The storm-track response to idealized SST perturbations in an aqua-planet GCM. *J. Atmos. Sci.*, **65**, 2842–2860, doi:10.1175/2008JAS2657.1.

Carton, J. A., and B. S. Giese, 2008: A reanalysis of ocean climate using Simple Ocean Data Assimilation (SODA). *Mon. Wea. Rev.*, **136**, 2999–3017, doi:10.1175/2007MWR1978.1.

Croci-Maspoli, M., C. Schwierz, and H. C. Davies, 2007: Atmospheric blocking: Space-time links to the NAO and PNA. *Climate Dyn.*, **29**, 713–725, doi:10.1007/s00382-007-0259-4.

Dijkstra, H., and M. Ghil, 2005: Low-frequency variability of the large-scale ocean circulation: A dynamical systems approach. *Rev. Geophys.*, **43**, RG3002, doi:10.1029/2002RG000122.

Feliks, Y., 1990: Isolated vortex evolution in 2 and 4 mode models. *Deep-Sea Res.*, **37A**, 571–591, doi:10.1016/0198-0149(90)90091-9.

——, M. Ghil, and E. Simonnet, 2004: Low-frequency variability in the midlatitude atmosphere induced by an oceanic thermal front. *J. Atmos. Sci.*, **61**, 961–981, doi:10.1175/1520-0469(2004)061<0961:LVITMA>2.0.CO;2.

——, ——, and ——, 2007: Low-frequency variability in the midlatitude baroclinic atmosphere induced by an oceanic thermal front. *J. Atmos. Sci.*, **64**, 97–116, doi:10.1175/JAS3780.1.

——, ——, and A. W. Robertson, 2010: Oscillatory climate modes in the eastern Mediterranean and their synchronization with the North Atlantic Oscillation. *J. Climate*, **23**, 4060–4079, doi:10.1175/2010JCLI3181.1.

——, ——, and ——, 2011: The atmospheric circulation over the North Atlantic as induced by the SST field. *J. Climate*, **24**, 522–542, doi:10.1175/2010JCLI3859.1.

——, A. Groth, A. W. Robertson, and M. Ghil, 2013: Oscillatory climate modes in the Indian monsoon, North Atlantic, and tropical Pacific. *J. Climate*, **26**, 9528–9544, doi:10.1175/JCLI-D-13-00105.1.

Flierl, G. R., 1978: Models of vertical structure and the calibration of two-layer models. *Dyn. Atmos. Oceans*, **2**, 341–381, doi:10.1016/0377-0265(78)90002-7.

Gaffney, S. J., A. W. Robertson, P. Smyth, S. J. Camargo, and M. Ghil, 2007: Probabilistic clustering of extratropical cyclones using regression mixture models. *Climate Dyn.*, **29**, 423–440, doi:10.1007/s00382-007-0235-z.

Gerber, E. P., and G. K. Vallis, 2009: On the zonal structure of the North Atlantic Oscillation and annular modes. *J. Atmos. Sci.*, **66**, 332–352, doi:10.1175/2008JAS2682.1.

Ghil, M., and A. W. Robertson, 2002: "Waves" vs. "particles" in the atmosphere's phase space: A pathway to long-range forecasting? *Proc. Natl. Acad. Sci. USA*, **99** (Supp.) 2493–2500, doi:10.1073/pnas.012580899.

——, and Coauthors, 2002: Advanced spectral methods for climatic time series. *Rev. Geophys.*, **40**, 1–41, doi:10.1029/2000RG000092.

Gray, B., and R. Madden, 1986: Aliasing in time-averaged tropical pressure data. *Mon. Wea. Rev.*, **114**, 1618, doi:10.1175/1520-0493(1986)114<1618:AITATP>2.0.CO;2.

Groth, A., and M. Ghil, 2011: Multivariate singular spectrum analysis and the road to phase synchronization. *Phys. Rev.*, **84E**, 036206, doi:10.1103/PhysRevE.84.036206.

Grotjahn, R., 1981: Stability properties of an arbitrarily oriented mean flow. *Tellus*, **33**, 188–200, doi:10.1111/j.2153-3490.1981.tb01743.x.

Haidvogel, D. B., A. Robinson, and E. Schulman, 1980: The accuracy, efficiency, and stability of three numerical models with application to open ocean problems. *J. Comput. Phys.*, **34**, 1–53, doi:10.1016/0021-9991(80)90111-4.

Held, I. M., 1983: Stationary and quasi-stationary eddies in the extratropical atmosphere: Theory. *Large-Scale Dynamical Processes in the Atmosphere*, B. J. Hoskins and R. P. Pearce, Eds., Academic Press, 127–168.

Hilmer, M., and T. Jung, 2000: Evidence for a recent change in the link between the North Atlantic Oscillation and Arctic sea ice export. *Geophys. Res. Lett.*, **27**, 989–992, doi:10.1029/1999GL010944.

Holton, J. R., and G. J. Hakim, 2012: *An Introduction to Dynamic Meteorology*. International Geophysics Series, Vol. 88, Academic Press, 552 pp.

Hoskins, B. J., I. N. James, and G. H. White, 1983: The shape, propagation and mean-flow interaction of large-scale weather systems. *J. Atmos. Sci.*, **40**, 1595–1612, doi:10.1175/1520-0469(1983)040<1595:TSPAMF>2.0.CO;2.

Hurrell, J. W., 1995: Decadal trends in the North Atlantic Oscillation. *Science*, **269**, 676–679, doi:10.1126/science.269.5224.676.

——, Y. Kushnir, G. Ottersen, and M. E. Visbeck, 2003: *The North Atlantic Oscillation: Climatic Significance and Environmental Impact. Geophys. Monogr.*, Vol. 134, Amer. Geophys. Union, 279 pp., doi:10.1029/GM134.

Jiang, S., F. Jin, and M. Ghil, 1995: Multiple equilibria, periodic, and aperiodic solutions in a wind-driven, double-gyre, shallow-water model. *J. Phys. Oceanogr.*, **25**, 764–786, doi:10.1175/1520-0485(1995)025<0764:MEPAAS>2.0.CO;2.

Johnson, N. C., S. B. Feldstein, and B. Tremblay, 2008: The continuum of Northern Hemisphere teleconnection patterns and a description of the NAO shift with the use of self-organizing maps. *J. Climate*, **21**, 6354–6371, doi:10.1175/2008JCLI2380.1.

Jones, P. D., T. Jonsson, and D. Wheeler, 1997: Extension to the North Atlantic Oscillation using early instrumental pressure observations from Gibraltar and south-west Iceland. *Int. J. Climatol.*, **17**, 1433–1450, doi:10.1002/(SICI)1097-0088(19971115)17:13<1433::AID-JOC203>3.0.CO;2-P.

Jung, T., M. Hilmer, E. Ruprecht, S. Kleppek, S. K. Gulev, and O. Zolina, 2003: Characteristics of the recent eastward shift of interannual NAO variability. *J. Climate*, **16**, 3371–3382, doi:10.1175/1520-0442(2003)016<3371:COTRES>2.0.CO;2.

Kalnay, E., and Coauthors, 1996: The NCEP/NCAR 40-Year Reanalysis Project. *Bull. Amer. Meteor. Soc.*, **77**, 437–471, doi:10.1175/1520-0477(1996)077<0437:TNYRP>2.0.CO;2.

Keppenne, C. L., and M. Ghil, 1993: Adaptive filtering and prediction of noisy multivariate signals: An application to subannual variability in atmospheric angular momentum. *Int. J. Bifurcation Chaos*, **3**, 625–634, doi:10.1142/S0218127493000520.

Lau, N.-C., 1988a: Variability of the observed midlatitude storm tracks in relation to low-frequency changes in the circulation pattern. *J. Atmos. Sci.*, **45**, 2718–2743, doi:10.1175/1520-0469(1988)045<2718:VOTOMS>2.0.CO;2.

——, 1988b: Variability of the observed midlatitude storm tracks in relation to low-frequency changes in the circulation pattern. *J. Atmos. Sci.*, **45**, 2718–2743, doi:10.1175/1520-0469(1988)045<2718:VOTOMS>2.0.CO;2.

Lindzen, R. S., and S. Nigam, 1987: On the role of sea surface temperature gradients in forcing low-level winds and convergence in the tropics. *J. Atmos. Sci.*, **45**, 2440–2458.

Liu, J.-W., S.-P. Zhang, and S.-P. Xie, 2013: Two types of surface wind response to the East China Sea Kuroshio front. *J. Climate*, **26**, 8616–8627, doi:10.1175/JCLI-D-12-00092.1.

Lorenz, E. N., 1967: *The Nature and Theory of the General Circulation of the Atmosphere*. World Meteorological Organization, 161 pp.

Luo, D., and T. Gong, 2006: A possible mechanism for the eastward shift of interannual NAO action centers in last three decades. *Geophys. Res. Lett.*, **33**, L24815, doi:10.1029/2006GL027860.

——, J. Cha, and S. B. Feldstein, 2012: Weather regime transitions and the interannual variability of the North Atlantic Oscillation. Part I: A likely connection. *J. Atmos. Sci.*, **69**, 2329–2346, doi:10.1175/JAS-D-11-0289.1.

Madden, R. A., and R. H. Jones, 2001: A quantitative estimate of the effect of aliasing in climatological time series. *J. Climate*, **14**, 3987–3993, doi:10.1175/1520-0442(2001)014<3987:AQEOTE>2.0.CO;2.

Mann, M. E., and J. M. Lees, 1996: Robust estimation of background noise and signal detection in climatic time series. *Climatic Change*, **33**, 409–445, doi:10.1007/BF00142586.

Miles, J. W., 1964: Baroclinic instability of the zonal wind. *Rev. Geophys.*, **2**, 155–176, doi:10.1029/RG002i001p00155.

Nakamura, H., T. Sampe, A. Goto, W. Ohfuchi, and S.-P. Xie, 2008: On the importance of midlatitude oceanic frontal zones for the mean state and dominant variability in the tropospheric circulation. *Geophys. Res. Lett.*, **35**, L15709, doi:10.1029/2008GL034010.

Namias, J., 1968: Long range weather forecasting—History, current status, and outlook. *Bull. Amer. Meteor. Soc.*, **49**, 438–470.

Pedlosky, J., 1982: *Geophysical Fluid Dynamics*. Springer-Verlag, 636 pp.

Plaut, G., and R. Vautard, 1994: Spells of low-frequency oscillations and weather regimes in the Northern Hemisphere. *J. Atmos. Sci.*, **51**, 210–236, doi:10.1175/1520-0469(1994)051<0210:SOLFOA>2.0.CO;2.

Robertson, A. W., and W. Metz, 1989: Three-dimensional linear instability of persistent anomalous large-scale flows. *J. Atmos. Sci.*, **46**, 2783–2801, doi:10.1175/1520-0469(1989)046<2783:TDLIOP>2.0.CO;2.

——, and ——, 1990: Transient-eddy feedbacks derived from linear theory and observations. *J. Atmos. Sci.*, **47**, 2743–2764, doi:10.1175/1520-0469(1990)047,2743:TEFDFL.2.0.CO;2.

Robinson, A. R., and J. C. McWilliams, 1974: The baroclinic instability of the open ocean. *J. Phys. Oceanogr.*, **4**, 281–294, doi:10.1175/1520-0485(1974)004<0281:TBIOTO>2.0.CO;2.

Rogers, J. C., 1997: North Atlantic storm track variability and its association to the North Atlantic Oscillation and climate variability of northern Europe. *J. Climate*, **10**, 1635–1647, doi:10.1175/1520-0442(1997)010<1635:NASTVA>2.0.CO;2.

Scaife, A. A., and Coauthors, 2014: Skillful long-range prediction of European and North American winters. *Geophys. Res. Lett.*, **41**, 2514–2519, doi:10.1002/2014GL059637.

Shutts, G. J., 1983: The propagation of eddies in diffluent jetstreams: Eddy vorticity forcing of 'blocking' flow fields. *Quart. J. Roy. Meteor. Soc.*, **109**, 737–761, doi:10.1002/qj.49710946204.

Simmons, A. J., and B. J. Hoskins, 1978: The life cycles of some nonlinear baroclinic waves. *J. Atmos. Sci.*, **35**, 414–432, doi:10.1175/1520-0469(1978)035<0414:TLCOSN>2.0.CO;2.

Simonnet, E., M. Ghil, and H. Dijkstra, 2005: Homoclinic bifurcations in the quasi-geostrophic double-gyre circulation. *J. Mar. Res.*, **63**, 931–956, doi:10.1357/002224005774464210.

Speich, S., H. Dijkstra, and M. Ghil, 1995: Successive bifurcations in a shallow-water model applied to the wind-driven ocean circulation. *Nonlinear Processes Geophys.*, **2**, 241–268, doi:10.5194/npg-2-241-1995.

Wallace, J., and D. Gutzler, 1981: Teleconnections in the geopotential height field during the Northern Hemisphere winter. *Mon. Wea. Rev.*, **109**, 784–812, doi:10.1175/1520-0493(1981)109<0784:TITGHF>2.0.CO;2.

Wang, X., and Coauthors, 2011: Trends and low-frequency variability of storminess over western Europe, 1878–2007. *Climate Dyn.*, **37**, 2355–2371, doi:10.1007/s00382-011-1107-0.

Woollings, T., A. Hannachi, and B. Hoskins, 2010a: Variability of the North Atlantic eddy-driven jet stream. *Quart. J. Roy. Meteor. Soc.*, **136**, 856–868, doi:10.1002/qj.625.

——, B. Hoskins, M. Blackburn, D. Hassell, and K. Hodges, 2010b: Storm track sensitivity to sea surface temperature resolution in a regional atmosphere model. *Climate Dyn.*, **35**, 341–353, doi:10.1007/s00382-009-0554-3.